

Higgs pair production in vector-boson fusion at the LHC and beyond

Fady Bishara^{a,1}, Roberto Contino^{b,2,3,4}, Juan Rojo^{c,5,6}

¹Rudolf Peierls Centre for Theoretical Physics, 1 Keble Road, University of Oxford, UK

²Scuola Normale Superiore, Pisa and INFN Pisa, Italy

³Institut de Théorie des Phénomènes Physiques, EPFL, Lausanne, Switzerland

⁴Theoretical Physics Department, CERN, Geneva, Switzerland

⁵Department of Physics and Astronomy, VU University Amsterdam, De Boelelaan 1081, NL-1081, HV Amsterdam, The Netherlands

⁶Nikhef, Science Park 105, NL-1098 XG Amsterdam, The Netherlands

Abstract The production of pairs of Higgs bosons at hadron colliders provides unique information on the Higgs sector and on the mechanism underlying electroweak symmetry breaking (EWSB). Most studies have concentrated on the gluon fusion production mode which has the largest cross section. However, despite its small production rate, the vector-boson fusion channel can also be relevant since even small modifications of the Higgs couplings to vector bosons induce a striking increase of the cross section as a function of the invariant mass of the Higgs boson pair. In this work, we exploit this unique signature to propose a strategy to extract the $hhVV$ quartic coupling and provide model-independent constraints on theories where EWSB is driven by new strong interactions. We take advantage of the higher signal yield of the $b\bar{b}b\bar{b}$ final state and make extensive use of jet substructure techniques to reconstruct signal events with a boosted topology, characteristic of large partonic energies, where each Higgs boson decays to a single collimated jet. Our results demonstrate that the $hhVV$ coupling can be measured with 45% (20%) precision at the LHC for $\mathcal{L} = 300$ (3000) fb^{-1} , while a 1% precision can be achieved at a 100 TeV collider.

1 Introduction

Following the discovery of the Higgs boson in 2012 [1, 2], the measurement of its couplings to the other Standard Model (SM) particles has become one of the main goals of the LHC programme. In this respect, double Higgs production provides a unique handle, in particular since it allows the extraction of the trilinear Higgs self-coupling λ . In addition to constraining λ , in the vector-boson fusion (VBF) channel double Higgs production also probes the strength of the Higgs non-linear interactions with vector bosons at high energies. This process can thus help establish the nature of the Higgs boson, whether it is a composite or elementary state, and whether or not it emerges as a Nambu-Goldstone boson (NGB) of some new dynamics at the TeV scale [3, 4, 5].

Many scenarios of new physics Beyond the SM (BSM) generically predict enhanced cross sections for Higgs pair production with or without the resonant production of new intermediate states, see for example Refs. [6, 7, 8, 9, 10, 11, 12, 13, 14, 15, 16, 17, 18, 19, 20]. For this reason, searches for Higgs pair production at the LHC by ATLAS and CMS have already started at 8 TeV [21, 22, 23, 24, 25] and 13 TeV [26, 27, 28, 29], and will continue during Runs II and III, as well as at the High-Luminosity LHC (HL-LHC) upgrade with 3 ab^{-1} of integrated luminosity. On the other hand, in the SM the small production rates make a measurement of Higgs pair production extremely challenging even at the HL-LHC, and the ultimate accuracy could only be achieved at a future 100 TeV hadron collider [30, 31, 32, 33, 34, 17].

Similarly to single Higgs production, the dominant mechanism for Higgs pair production is the gluon-fusion mode [35]. This channel has been extensively studied in the literature and several final states have been considered, including $b\bar{b}\gamma\gamma$, $b\bar{b}\tau^+\tau^-$, $b\bar{b}W^+W^-$ and $b\bar{b}b\bar{b}$ (for a list of feasibility studies, see for example Refs. [36, 37, 38, 39, 30, 40, 41, 42, 43, 17]). Working in the infinite top mass approximation, the gluon-fusion di-Higgs production cross section was calculated at NLO in [44] and NNLO in [45]. The resummation of soft-gluon emissions was performed at NNLL in [46, 47]. Beyond the $m_t \rightarrow \infty$ limit, the impact of top quark mass effects on NLO QCD corrections was first determined in [48] through a reweighting technique based on an approximate two-loop matrix element and by [49, 50] in a

^aE-mail: fady.bishara@physics.ox.ac.uk

^bE-mail: roberto.contino@sns.it

^cE-mail: j.rojo@vu.nl

$1/m_t$ expansion. Recently, the full NLO calculation was performed by [51]. Matching the fixed order computations to a parton shower was done at LO in [52] and at NLO in [53].

Recent studies indicate that Higgs pair production in gluon-fusion at the HL-LHC will allow the extraction of the Higgs self-coupling λ with $\mathcal{O}(1)$ accuracy, with details varying with the analysis and the specific final state, see Refs. [54,55,56,57,58] for the latest ATLAS and CMS estimates, as well as [38,59,30,60,17].

Higgs pairs can also be produced in the VBF channel [3,4,61,62,63,64] where a soft emission of two vector bosons from the incoming protons is followed by the hard $VV \rightarrow hh$ scattering, with $V = W, Z$. In the SM, the VBF inclusive cross section at 14 TeV is around 2 fb – more than one order of magnitude smaller than in gluon fusion. QCD corrections give a 10% increase and have been computed at NLO in Refs. [65,53] and at NNLO in Ref. [63]. Production in association with W or Z bosons, known as the Higgsstrahlung process [66,65,67], or with top quark pairs [68], exhibit even smaller cross sections.

Despite its small rate, Higgs pair production via VBF is quite interesting since even small modifications of the SM couplings can induce a striking increase of the cross section as a function of the di-Higgs mass. Specific models leading to this behaviour are, for instance, those where the Higgs is a composite pseudo-NGB (pNGB) of new strong dynamics at the TeV scale [69]. In these theories, the Higgs anomalous couplings imply a growth of the $VV \rightarrow hh$ cross section with the partonic center-of-mass energy, $\hat{\sigma} \propto \hat{s}/f^4$, where f is the pNGB decay constant [3]. This enhanced sensitivity to the underlying strength of the Higgs interactions makes double Higgs production via VBF a key process to test the nature of the electroweak symmetry breaking dynamics and to constrain the $hhVV$ quartic coupling. A first study of double Higgs production via VBF at the LHC was performed in Ref. [4], for a mass $m_h = 180$ GeV, by focusing on the $4W$ final state. Following the discovery of the Higgs boson, more studies of the $hhjj$ process at the LHC were presented in Refs. [61,62,64,70].

In this work, we revisit the feasibility of VBF Higgs pair production at the LHC and focus on the $hh \rightarrow b\bar{b}b\bar{b}$ final state. While this final state benefits from increased signal yields due to the large branching fraction of Higgs bosons to bottom quarks, $\text{BR}(H \rightarrow b\bar{b}) = 0.582$ in the SM [35], it also suffers from overwhelming large QCD multi-jet backgrounds. In this respect, the remarkable VBF topology, characterized by two forward jets well separated in rapidity and with a large invariant mass, together with a reduced hadronic activity in the central region, provides an essential handle to disentangle signal events from the QCD background. Additionally, the di-Higgs system will acquire a substantial boost in the presence of BSM dynamics. It is thus advantageous to resort to jet substructure techniques [71] in order to fully exploit the high-energy limit and optimize the signal significance.

We will thus focus on the kinematic region where the invariant mass of the Higgs pair, m_{hh} , is large because modifications of the couplings between the Higgs and vector bosons cause the tail of this distribution to become harder in the signal whereas the background is not modified. Therefore, this region exhibits the highest sensitivity to the modified Higgs couplings and in particular to the deviations in the $hhVV$ quartic coupling c_{2V} . Given that for large m_{hh} the Higgs bosons can be produced boosted, improved discrimination can be achieved using jet substructure, and to this end we use scale-invariant tagging [10,43] to smoothly combine the resolved, intermediate and boosted topologies.

Our analysis takes into account all the main reducible and irreducible backgrounds: QCD multijet production, Higgs production via gluon fusion (where additional radiation can mimic the VBF topology), and top quark pair production. We pay special attention to the role of light and charm jets being misidentified as b -jets which can contribute sizeably to the total background yield. For instance, in the $gg \rightarrow hh \rightarrow b\bar{b}b\bar{b}$ channel, the $2b2j$ background is comparable to the $4b$ component [43].

We quantify the constraints on the Higgs quartic coupling c_{2V} that can be obtained from VBF di-Higgs production at the LHC 14 TeV with $\mathcal{L} = 300\text{fb}^{-1}$ and 3000fb^{-1} as well as at a Future Circular Collider (FCC) with a centre-of-mass energy of 100 TeV and a total luminosity of 10ab^{-1} . We find that, despite the smallness of the production cross sections, the LHC with 300fb^{-1} can already constrain the $hhVV$ coupling with an accuracy of $^{+45\%}_{-37\%}$ around its SM value at the $1\text{-}\sigma$ level, which is further reduced to $^{+19\%}_{-15\%}$ at the HL-LHC and down to the 1% level at the FCC. Our results strongly motivate that searches for VBF Higgs pair production at the LHC should already start during Run II.

The structure of this paper is as follows. In Sec. 2 we present the general parametrization of the Higgs couplings which we adopt and review its impact on VBF Higgs pair production. Then in Sec. 3, we discuss the analysis strategy used to disentangle the signal from the background events in the $b\bar{b}b\bar{b}$ final state. Our main results are presented in Sec. 4, where we quantify the potential of the VBF di-Higgs process to measure the $hhVV$ coupling at various colliders and discuss the validity of the effective field theory expansion. Finally in Sec. 5, we conclude and discuss how our analysis strategy could be applied to related processes. Technical details are collected in three appendices which describe the Monte Carlo event generation of signal and background events (Appendix A), the fits to the tail of the m_{hh}

distribution for backgrounds (Appendix B), and the validation studies of the QCD multijet event generation (Appendix C).

2 Higgs pair production via vector boson fusion at hadron colliders

We begin by reviewing the theoretical framework for Higgs pair production via vector boson fusion in hadronic collisions. First, we introduce a general parametrization of the Higgs couplings in the effective field theory (EFT) framework. Then, we turn to consider the values that these couplings take in specific models. Finally, we briefly discuss the validity of the EFT approximation and the possible contribution of heavy resonances to this process.

2.1 General parametrization of Higgs couplings

Following Ref. [4], we introduce a general parametrization of the couplings of a light Higgs-like scalar h to the SM vector bosons and fermions. At energies much lower than the mass scale of any new resonance, the theory is described by an effective Lagrangian obtained by making a derivative expansion. Under the request of custodial symmetry, the three NGBs associated with electroweak symmetry breaking parametrize the coset $SO(4)/SO(3)$ and can be fitted into a 2×2 matrix

$$\Sigma = e^{i\sigma^a \pi^a / v}, \quad (1)$$

with $v = 246$ GeV the Higgs vacuum expectation value. Assuming that the couplings of the Higgs boson to SM fermions scale with their masses and do not violate flavor, the resulting effective Lagrangian in [4] can be parametrized as

$$\begin{aligned} \mathcal{L} \supset & \frac{1}{2}(\partial_\mu h)^2 - V(h) + \frac{v^2}{4} \text{Tr}(D_\mu \Sigma^\dagger D^\mu \Sigma) \left[1 + 2c_V \frac{h}{v} + c_{2V} \frac{h^2}{v^2} + \dots \right] \\ & - m_i \bar{\psi}_{Li} \Sigma \left(1 + c_\psi \frac{h}{v} + \dots \right) \psi_{Ri} + \text{h.c.}, \end{aligned} \quad (2)$$

where $V(h)$ denotes the Higgs potential,

$$V(h) = \frac{1}{2} m_h^2 h^2 + c_3 \frac{1}{6} \left(\frac{3m_h^2}{v} \right) h^3 + c_4 \frac{1}{24} \left(\frac{3m_h^2}{v^2} \right) h^4 + \dots \quad (3)$$

The parameters c_V , c_{2V} , c_ψ , c_3 , and c_4 are in general arbitrary coefficients, normalized so that they equal 1 in the SM. The Higgs mass is fixed to be $m_h = 125$ GeV [72].

As the notation in Eq. (2) indicates, the coefficients c_V , c_{2V} , and c_3 control the strength of the hVV , $hhVV$ and hhh couplings, respectively. The coefficients c_ψ and c_4 instead modify the Higgs coupling to fermions and quartic self interaction. Thus, they do not affect the double-Higgs production cross section in the VBF channel. In Fig. 1, we show the tree-level Feynman diagrams, in the unitary gauge, that contribute to Higgs pair production in the vector-boson fusion channel at hadron colliders. In terms of the general parametrization of Eq. (2), the left, middle, and right diagrams scale with c_{2V} , c_V^2 , and $c_V c_3$, respectively.

In the SM, a cancellation dictated by perturbative unitarity occurs between the first and second diagrams. This is best understood by describing the process as a slow emission of the vector bosons by the protons followed by their hard scattering into a pair of Higgs bosons [73]. For generic values of c_V and c_{2V} , the amplitude of the partonic scattering $VV \rightarrow hh$ grows with the energy $\sqrt{\hat{s}}$ until the contribution from the new states at the cutoff scale Λ unitarizes it. The leading contribution in the energy range $m_W \ll \sqrt{\hat{s}} \equiv m_{hh} \ll \Lambda$ comes from the scattering of longitudinal vector bosons and is given by

$$\mathcal{A}(V_L V_L \rightarrow hh) \simeq \frac{\hat{s}}{v^2} (c_{2V} - c_V^2), \quad (4)$$

up to $\mathcal{O}(m_W^2/\hat{s})$ and $\mathcal{O}(\hat{s}/\Lambda^2)$ corrections. In scenarios with $c_{2V} \neq c_V^2$, the growth of the partonic cross section with \hat{s} thus provides a smoking-gun signature for the presence of BSM dynamics [3].

In the parametrization of Eq. (2), the amplitude for the process $pp \rightarrow hhjj$ can be decomposed as follows

$$\mathcal{A} = \tilde{A} c_V^2 + \tilde{B} c_{2V} + \tilde{C} c_V c_3, \quad (5)$$

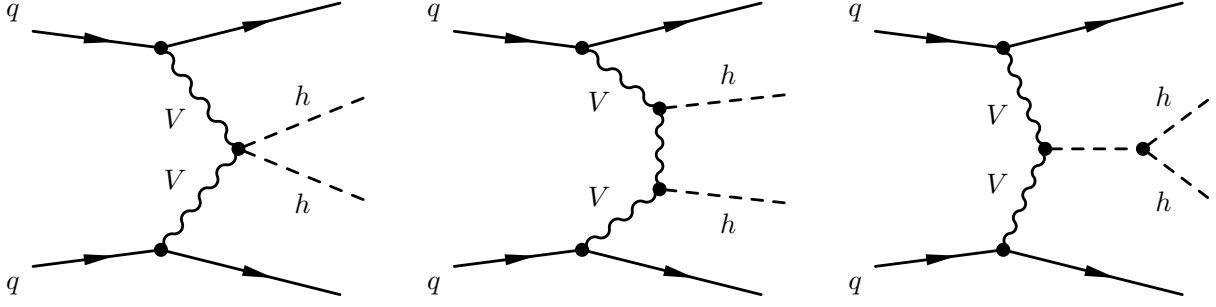


Fig. 1 Tree-level Feynman diagrams contributing to Higgs pair production via VBF. In terms of Eq. (2), the left, middle, and right diagrams scale with c_{2V} , c_V^2 , and $c_V c_3$, respectively.

where \tilde{A} , \tilde{B} , and \tilde{C} are numerical coefficients. In the present work, we will focus on the quartic coupling c_{2V} and set c_V and c_3 to their SM values. This is justified for c_V since the ATLAS and CMS measurements of Higgs production cross sections, when analysed in the context of a global fit of Higgs properties [74, 75, 76] typically set bounds on $c_V - 1$ at the level of 10 – 20%, depending on the specific assumptions made – see for example [77, 78, 79] and references therein. Tighter limits on c_V can be derived from electroweak precision tests in the absence of additional BSM contributions [80].

On the other hand, the trilinear Higgs coupling c_3 (where $c_3 = \lambda/\lambda_{\text{SM}}$) only has loose experimental constraints so far. As an illustration, a recent ATLAS search for non-resonant Higgs pair production at 13 TeV in the $b\bar{b}b\bar{b}$ final state [27] translates into the bound $\sigma(hh)/\sigma_{\text{SM}}(hh) \lesssim 27$ at the 95% confidence level. Achieving $\mathcal{O}(1)$ precision in the measurement of c_3 will thus most likely require the full HL-LHC statistics. Focusing on VBF production, as anticipated and further discussed in the following, gaining sensitivity to c_{2V} is achieved by reconstructing events with large values of m_{hh} . In this kinematic region, it turns out that the sensitivity to c_3 is reduced, indicating that our analysis is not optimal to probe the Higgs trilinear coupling. For these reasons, setting $c_V = c_3 = 1$ is a good approximation in the context of the present analysis. We can then define

$$\delta_{c_{2V}} \equiv c_{2V} - 1, \quad (6)$$

and this way the total cross section will be parametrized as

$$\sigma = \sigma_{\text{SM}} (1 + A \delta_{c_{2V}} + B \delta_{c_{2V}}^2). \quad (7)$$

However, while setting $c_3 = 1$ is a very good approximation, fixing $c_V = 1$ is not as equally well justified. In particular, it would be more prudent to treat c_V as a Gaussian distributed nuisance parameter centred around its SM value with a width corresponding to the current experimental precision. To do this, a similar expression to Eq. (7) above can be derived by neglecting the sub-leading effects involving c_3 . In this case, Eq. (7) is replaced by

$$\sigma \approx \sigma_{\text{SM}} c_V^4 \left(1 + A \left[\frac{c_{2V}}{c_V^2} - 1 \right] + B \left[\frac{c_{2V}}{c_V^2} - 1 \right]^2 \right). \quad (8)$$

We will use this expression to evaluate the impact of c_V on the derived bounds on $\delta_{c_{2V}}$ at the end of Sec. 4. The values of the SM cross section σ_{SM} and of the parameters A , B are reported in Table 1 for $\sqrt{s} = 14$ and 100 TeV, both after acceptance cuts and after applying all the analysis cuts as discussed in Sec. 3 – see Appendix D for the values of the parameters in bins of m_{hh} . We will make extensive use of this parametrization in Sec. 4 where we present our results in terms of the sensitivity on $\delta_{c_{2V}}$. Note that the value of A and B increase after imposing all cuts precisely because they have been optimized to enhance the sensitivity on c_{2V} .

Although we do not attempt to extract c_3 with our analysis, it is still interesting to discuss the dependence of the total cross section on this parameter. By fixing $c_V = c_{2V} = 1$ and defining $\delta_{c_3} \equiv c_3 - 1$, the cross section can now be parametrized as

$$\sigma = \sigma_{\text{SM}} (1 + C \delta_{c_3} + D \delta_{c_3}^2). \quad (9)$$

The coefficients C and D are also reported in Table 1. As opposed to the previous case, now their values decrease after applying the full set of cuts, reflecting that the sensitivity on c_3 is suppressed by our analysis which aimed at

\sqrt{s}	Cuts	σ_{SM} [fb]	A	B	C	D
14TeV	Acceptance	0.010	-5.19	29.5	-0.939	0.854
	All	0.0018	-8.18	67.5	-0.699	0.325
100TeV	Acceptance	0.20	-9.18	306	-0.699	0.584
	All	0.030	-20.7	1080	-0.516	0.251

Table 1 Coefficients of Eqs. (7) and (9) as obtained through a fit of Montecarlo points. The cuts are listed in Table 2 and Eqs. (15)–(17).

measuring c_{2V} . Extracting c_3 would require retaining the events close to the hh threshold, but this kinematic region is totally dominated by the background and turns out to be of little use. A measurement of the Higgs trilinear coupling in the VBF channel using the $b\bar{b}b\bar{b}$ final state thus does not seem feasible even at the FCC. Though, other final states might exhibit better prospects at 100 TeV.

2.2 Models

The Lagrangian of Eq. (2), with arbitrary values of the coefficients c_V , c_{2V} , c_ψ , c_3 and c_4 , describes a generic light scalar, singlet of the custodial symmetry, independently of its role in the electroweak symmetry breaking. In specific UV models, however, the coefficients c_i are generally related to each other and their values are subject to constraints which depend on whether the Higgs-like boson h is part of an $SU(2)_L$ doublet. For example, in the SM, all the parameters in Eq. (2) are equal to 1 and terms denoted by the ellipses vanish. In this case, the scalar h and the three NGBs combine to form a doublet of $SU(2)_L$ which is realized linearly at high energies.

Composite Higgs theories are another example where the electroweak symmetry is realized linearly in the UV, though, in this case non-linearities in the Higgs interactions can be large and are controlled by the ratio $\xi \equiv v^2/f^2$, where f is the pNGB decay constant. For instance, minimal $SO(5)/SO(4)$ models [81, 82] predict

$$c_V = \sqrt{1 - \xi}, \quad c_{2V} = 1 - 2\xi. \quad (10)$$

On the other hand, the value of the Higgs trilinear coupling is not determined by the coset structure alone, and depends on how the Higgs potential is specifically generated. For instance, in the MCHM5 model with fermions transforming as vector representations of $SO(5)$ [82], the Higgs potential is entirely generated by loops of SM fields and the Higgs trilinear coupling is predicted to be

$$c_3 = \frac{1 - 2\xi}{\sqrt{1 - \xi}}. \quad (11)$$

A precision model-independent determination of c_{2V} would thus provide stringent constraints on a number of BSM scenarios. To begin with, if the Higgs boson belongs to an electroweak doublet, as suggested by the LHC data, and the modifications to its couplings are small, then the values of c_{2V} and c_V are in general predicted to be correlated [3, 5]:

$$\delta_{c_{2V}} \simeq 2\delta_{c_V^2}, \quad (12)$$

where $\delta_{c_V^2} \equiv c_V^2 - 1$. This follows because there is a single dimension-6 effective operator (O_H in the basis of Ref. [3]) which controls the shift in both couplings. Therefore, a high-precision measurement of c_{2V} can test whether the Higgs boson belongs to a doublet in case a deviation is observed in c_V [5].

Another interesting case is the scenario where the Higgs-like boson is not part of a doublet, and in fact does not play any role in the electroweak symmetry breaking mechanism, known as the light dilaton scenario [83, 84, 85, 86, 87, 88]. In this model, invariance under dilatations implies $\delta_{c_{2V}} = \delta_{c_V^2}$, a condition that can be tested if the two couplings in Eq. (12) can be measured with comparable precision. Moreover, comparing c_{2V} and c_V can also provide information on the coset structure in the case of a composite NGB Higgs [5].

A large variety of BSM scenarios also exist where the Higgs trilinear coupling receives large modifications while the value of the other couplings are close to the SM prediction. Higgs portal models fall in this class, see for example the discussion in [36, 17] and also [89, 90]. However, since our analysis is not sensitive to c_3 , we will not consider these scenarios any further and will always assume $\delta_{c_3} = 0$.

In the following, we will take as a representative benchmark scenario a model with $c_{2V} = 0.8$ corresponding to $\delta_{c_{2V}} = -0.2$, with the other couplings set to their SM values, namely $\delta_{c_V} = \delta_{c_3} = 0$.

2.3 Validity range of the effective theory

As discussed above, and shown by Eq. (4), the amplitude of the partonic scattering $VV \rightarrow hh$ grows with the energy in the EFT described by Eq. (2). However, this behavior holds only below the typical mass scale of new BSM states, i.e. below the cutoff scale Λ of the effective theory. When the invariant mass of the di-Higgs system becomes large enough, the EFT approximation breaks down and it becomes necessary to take into full account the contribution from the exchange of new states, such as vector and scalar resonances. These resonances eventually tame the growth of the scattering amplitude at large energies to be consistent with perturbative unitarity bounds. In the context of composite Higgs scenarios the impact of resonances on VV scattering has been explored for instance in [91, 92, 93, 94, 95, 96].

While we do not include the effect of such resonances in this work, we will report the sensitivity on $\delta_{c_{2V}}$ as a function of the maximum value of the invariant mass of the di-Higgs system (see Fig. 13 in Sec. 4), as suggested by Ref. [97]. This comparison allows one to assess the validity of the EFT description once an estimate of c_{2V} is provided in terms of the masses and couplings of the UV dynamics. The result of this analysis – which is discussed in detail at the end of Sec. 4 – confirms that the EFT is valid over the full range of m_{hh} that is used to derive limits on $\delta_{c_{2V}}$. The explicit inclusion of scalar and vector resonances and their phenomenological implications for Higgs pair production via VBF is left for future work.

3 Analysis strategy

In this section we present our analysis of double Higgs production via VBF. First, we discuss how signal and background events are reconstructed and classified. This includes a description of the jet reconstruction techniques adopted, the b -tagging strategy, and the event categorisation in terms of jet substructure. Then we illustrate the various selection cuts imposed to maximize the signal significance, in particular the VBF cuts, as well as the method used to identify the Higgs boson candidates. Finally, we present the signal and background event rates for the various steps of the analysis, and discuss how the signal cross-sections are modified when c_{2V} is varied as compared to its SM value.

3.1 Event reconstruction and classification

Signal and background events are simulated at leading-order (LO) by means of matrix-element generators and then processed through a parton shower (PS). The detailed description of the event generation of signal and backgrounds can be found in Appendix A. The dominant background is given by QCD multijet production, while other backgrounds, such as top-quark pair production and Higgs pair production via gluon-fusion, are much smaller. After the parton shower, events are clustered with FASTJET v3.0.1 [98] using the anti- k_t algorithm [99] with a jet radius $R = 0.4$.

The resulting jets are processed through a b -tagging algorithm, where a jet is tagged as b -jet with probability $\varepsilon(b\text{-tag})$ if it contains a b -quark with $p_T^b > 15$ GeV. In order to account for b -jet misidentification (fakes), jets which do not meet this requirement are also tagged as b -jets with probability $\varepsilon(c\text{-mistag})$ or $\varepsilon(q, g\text{-mistag})$ depending on whether they contain a c -quark or not. Only events with four or more jets, of which at least two must be b -tagged, are retained at this stage.

Fully exploiting the $b\bar{b}b\bar{b}$ final state requires efficient b -tagging capabilities, in both the resolved and boosted regimes as well as a good rejection of fakes. Both ATLAS and CMS have presented recent studies of their capabilities in terms of b -tagging and light-jet fake rejection for both topologies, see Refs. [100, 101, 102, 103, 104] and references therein. In the present study, we have considered two representative b -tagging working points:

$$\begin{aligned} \text{WP1 : } & \quad \varepsilon(b\text{-tag}) = 0.75, \quad \varepsilon(c\text{-mistag}) = 0.1, \quad \varepsilon(q, g\text{-mistag}) = 0.01, \\ \text{WP2 : } & \quad \varepsilon(b\text{-tag}) = 0.8, \quad \varepsilon(c\text{-mistag}) = 0.05, \quad \varepsilon(q, g\text{-mistag}) = 0.005. \end{aligned} \tag{13}$$

The first point is consistent with the current performance of ATLAS and CMS, and is the one adopted as baseline in this paper. The second working point is more optimistic and is intended to assess how much one could gain with a more efficient b -tagger. As our results will show (see Fig. 14), using WP2 leads to a marginal improvement in our analysis. For simplicity, we applied the efficiencies in Eq. 13 to a jet based on its constituents. This is sufficient for the purpose of the current analysis which is, namely, to demonstrate the sensitivity of double Higgs production via VBF to $\delta_{c_{2V}}$. Accordingly, we leave a detailed study of b -tagging including hadronization effects and p_T dependence to future studies.

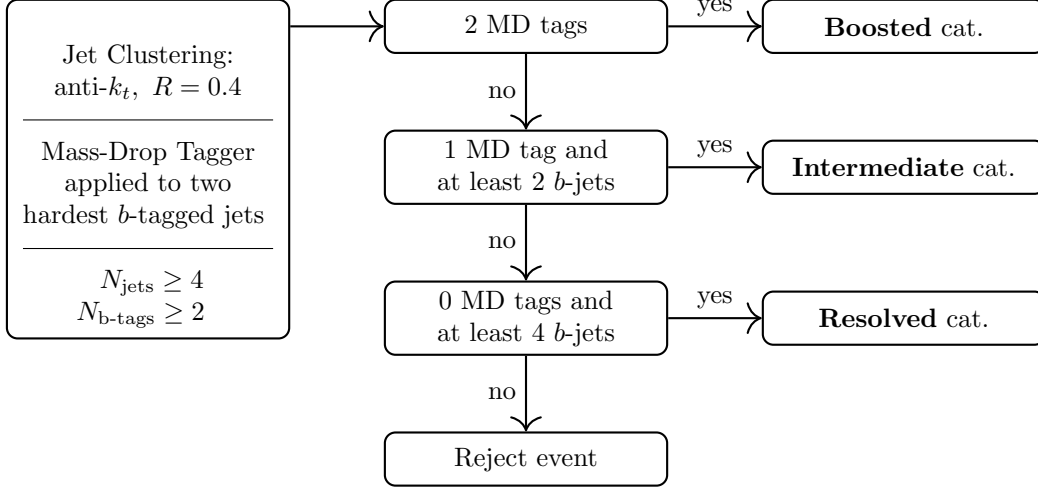


Fig. 2 Schematic representation of the analysis strategy adopted in this work.

Subsequently to b -tagging, events are classified through a scale-invariant tagging procedure [10,43]. This step is crucial to efficiently reconstruct the Higgs boson candidates and suppress the otherwise overwhelming QCD backgrounds while at the same time taking into account all the relevant final-state topologies. The basic idea of this method is to robustly merge three event topologies – *boosted*, *intermediate* and *resolved* – into a common analysis. This is particularly relevant for our study since, as discussed in Sec. 2, the degree of boost of the di-Higgs system strongly depends on the deviations of c_{2V} from its SM value.

This scale-invariant tagging strategy is schematically represented in Fig. 2. First of all, the b -tagged jets are ordered in p_T and the constituents of the hardest two jets are then re-clustered using the Cambridge/Aachen (C/A) algorithm [105] with $R_{C/A} = 1.2$. Each C/A jet is processed with the BDRS mass-drop (MD) tagger [106]. This jet-substructure tagger has two parameters: μ and y_{cut} . And, in this work, we set $\mu = 0.67$ and $y_{\text{cut}} = 0.09$ as in the original BDRS study. To determine if a given jet arises from the decay of a massive object, the last step of the clustering for jet j is undone, giving two subjets j_1 and j_2 which are ordered such that $m_{j_1} > m_{j_2}$. Then, if the two subjets satisfy the conditions

$$m_{j_1} \leq \mu \cdot m_j \quad \text{and} \quad \min(p_{Tj_1}^2, p_{Tj_2}^2) \Delta R_{j_1, j_2}^2 > y_{\text{cut}} \cdot m_j^2, \quad (14)$$

where $\Delta R_{j_1, j_2}$ is the angular separation between the two subjets, j is tagged as a jet with a mass drop. Else, the procedure is applied recursively to j_1 until a mass drop is found or the C/A jet is fully unclustered.

Jets are mass-drop tagged only if they satisfy the following additional requirement: at least two b -quarks must be contained within the jet, each of which with $p_{Tb} \geq 15$ GeV, and with a minimal angular separation $\Delta R_{bb} \geq 0.1$. The request of a second b -quark completes our b -tagging algorithm in the case of boosted jets. Other more sophisticated approaches to b -tagging could have been considered – e.g., using ghost-association between large- R MD-tagged jets and small- R b -tagged jets [43,23], or accounting for an efficiency which depends on the jet p_T [107]. The approach followed here is at the same time simple yet realistic enough for a first feasibility study with the caveat that a more complete analysis should treat b -tagging more in line with the actual performance of the ATLAS and CMS detectors (and in particular it should include a full detector simulation).

The use of the BDRS mass-drop tagger allows us to classify a given signal or background event under one of the three categories: boosted, if two mass-drop tags are present; intermediate, for an event with a single mass-drop tag; and resolved, if the event has no mass-drop tags. In the resolved category, events are only retained if they contain at least 4 b -tagged jets, while at least 2 b -tagged jets, in addition to the MD-tagged jet, are required in the intermediate one. By construction, this classification is exclusive, *i.e.*, each event is unambiguously assigned to one of the three categories. This exclusivity allows the consistent combination of the signal significance from the three separate categories.

Following the event categorisation, acceptance cuts to match detector coverage are applied to signal and background events. These cuts are listed in the upper part of Table 2, and have been separately optimized for the LHC 14 TeV and the FCC 100 TeV. We require the p_T of the light (b -tagged) jets to be larger than 25 GeV (25 GeV) at 14 TeV and than 40 GeV (35 GeV) at 100 TeV, respectively. Concerning the pseudo-rapidities of light and b -tagged jets, η_j and η_b , at the LHC the former is limited by the coverage of the forward calorimeters, while the latter is constrained by

		14 TeV	100 TeV
Acceptance cuts	p_{T_j} (GeV) \geq	25	40
	p_{T_b} (GeV) \geq	25	35
	$ \eta_j \leq$	4.5	6.5
	$ \eta_b \leq$	2.5	3.0
VBF cuts	$ \Delta y_{jj} \geq$	5.0	5.0
	m_{jj} (GeV) \geq	700	1000
	Central jet veto: $p_{T_{j_3}}$ (GeV) \leq	45	65

Table 2 Acceptance and VBF selection cuts applied to signal and background events after jet clustering and b -tagging. The central jet veto is applied on jets with pseudo-rapidity η_{j_3} in the interval $\eta_j^{\min} < \eta_{j_3} < \eta_j^{\max}$, where η_j^{\max} and η_j^{\min} are the pseudo-rapidities of the VBF-tagging jets.

the tracking region where b -tagging can be applied. At 100 TeV, we assume a detector with extended coverage of the forward region up to $|\eta|$ of 6.5 [108].

3.2 VBF selection cuts

Subsequently to the acceptance cuts, we impose a set of selection cuts tailored to the VBF topology which is characterized by two forward and very energetic jets with little hadronic activity between them. In particular, we cut on the rapidity separation $\Delta y_{jj} \equiv |y_j^{\text{lead}} - y_j^{\text{sublead}}|$ and the invariant mass m_{jj} of the two VBF-tagging jets, and impose a central jet veto (CJV) on the hardest non-VBF light jet in the central region. The VBF tagging jets are defined as the pair of light jets satisfying the acceptance cuts of Table 2 with the largest invariant mass m_{jj} . This definition is robust with respect to soft contamination from the underlying event (UE) and pile-up (PU) and to the contribution of b -jets mistagged as light jets.

Figure 3 shows the distribution of the rapidity separation $|\Delta y_{jj}|$ and invariant mass m_{jj} of the VBF tagging jets at 14 TeV and 100 TeV after the acceptance cuts. In each case, we show the results for the signal (SM and $c_{2V} = 0.8$ benchmark) and for the total background. The signal distributions exhibit the distinctive VBF topology, with two VBF tagging jets widely separated in rapidity and with a large invariant mass. This is in contrast with the backgrounds where both the Δy_{jj} and m_{jj} distributions peak at zero. In Fig. 3, as well as in the subsequent figures, kinematic distributions have been area-normalized and then rescaled by a common factor such that the largest bin in the plot is of unit height.

Based on the distributions of Fig. 3 we identified appropriate values of the VBF cuts, listed in Table 2 and represented in each panel by a vertical dash-dotted line. It is important to tailor these cuts to the specific center-of-mass energy, 14 TeV and 100 TeV, to avoid losing a substantial fraction of the signal events. One should also take into account that the large rapidity separation between the VBF tagging jets in signal events results from jets pairs with a large invariant mass, given that these two variables are strongly correlated [4]. This large separation in rapidity is especially useful in the $b\bar{b}b\bar{b}$ final state to trigger on signal events, providing a significant improvement compared to the same final state produced in gluon-fusion where triggering issues are more severe [42, 43].

Figure 3 clearly highlights that in order to maximize the acceptance of events with VBF topology – the detectors must have a good coverage of the forward region. This issue is particularly relevant at 100 TeV as illustrated in Fig. 4 which shows the pseudo-rapidity distribution of the most forward light jet. At 100 TeV, this peaks at around 5, so a detector instrumented only up to $|\eta| = 4.5$ would lose more than 50% of signal events. The discontinuity in the FCC case delineates the edge of the b -jet acceptance region, $|\eta| \leq 3$, above which no b -tagging is attempted and b -jets contribute to the light-jet yield.

Turning to the transverse momentum of the light jets, Fig. 5 shows the p_T distributions of the three hardest jets at 14 TeV and 100 TeV for SM signal events. One can see that while the leading jet is typically quite hard, the subleading ones are rather soft. It is thus important to avoid imposing a too stringent cut in p_T , in order not to suppress the signal. Fortunately, in contrast from the gluon-fusion process, adopting a soft p_T cut is not a problem since triggering can be performed based on the VBF topology. Comparing the p_T distributions at 14 TeV and 100 TeV, their shapes turn out to be rather similar, shifted towards larger values at 100 TeV. This justifies the harder p_T cut in this case (see Table 2), also required to reduce the contamination from UE and PU.

As mentioned above, another characteristic feature of VBF production is a reduced hadronic activity in the central region between the two VBF-tagging jets. This follows because the latter are not colour-connected since the production of the central system only involves electroweak bosons. For this reason, a CJV cut is commonly imposed in VBF

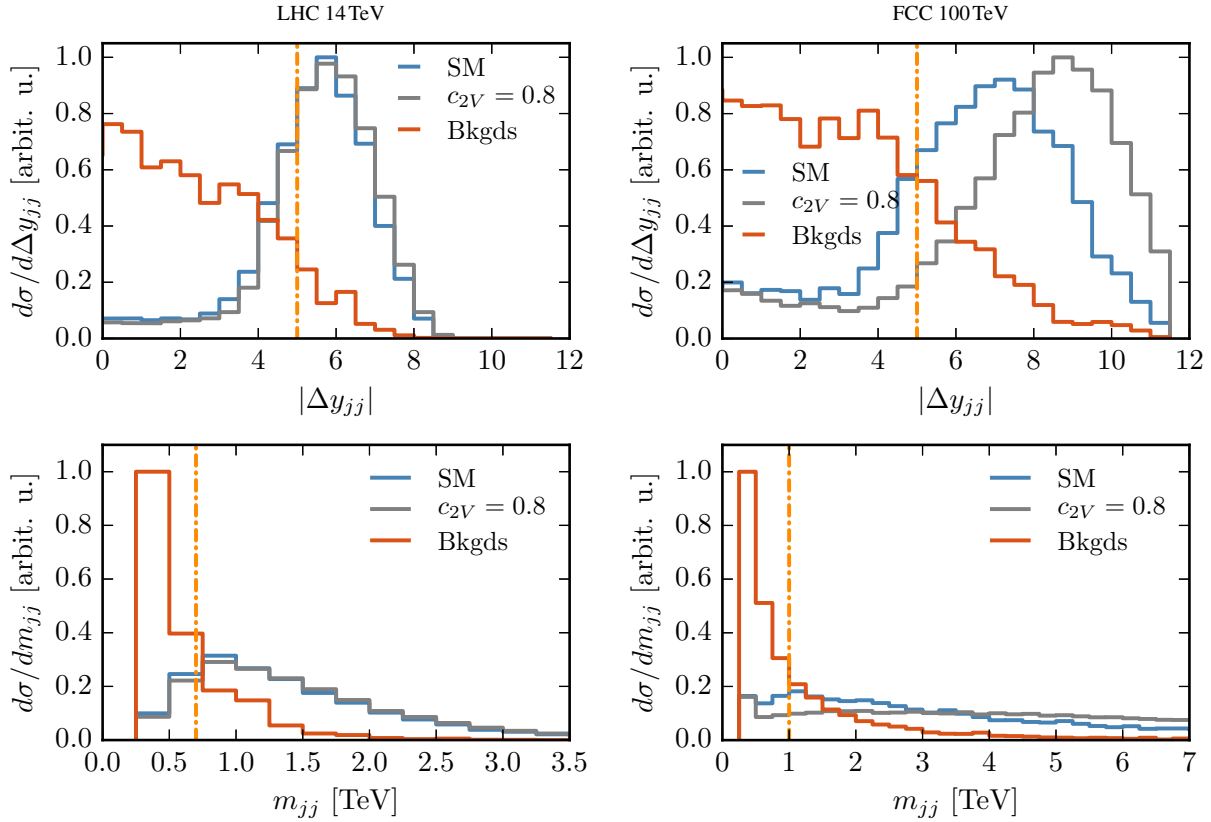


Fig. 3 Distribution of the rapidity separation $|\Delta y_{jj}|$ (upper) and the invariant mass m_{jj} (bottom panels) of the VBF tagging jets at 14 TeV (left) and 100 TeV (right panels), for signal (SM and $c_{2V} = 0.8$) and background events after the acceptance cuts. The vertical line indicates the value of the corresponding cut from Table 2. The distributions have been area-normalized and rescaled by a common factor.

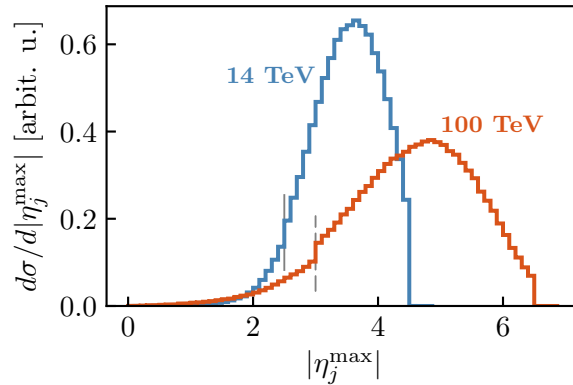


Fig. 4 Distribution of the pseudo-rapidity $|\eta_j^{\max}|$ of the most forward light jet at 14 TeV and 100 TeV. Both curves have a discontinuity at the edge of the corresponding b-tagging region which is delineated by the solid (dashed) grey vertical lines in the case of 14 (100) TeV. This discontinuity is more clearly visible in the 100 TeV curve and is purely due to combinatorics.

analyses. This cut vetoes light jets, with pseudo-rapidity η_{j_3} , lying between those of the VBF-tagging jets, $\eta_j^{\max} > \eta_{j_3} > \eta_j^{\min}$, above a given p_T threshold.

The effect of the CJV is illustrated in Fig. 6 where we show the distribution of the p_T of the 3rd light jet, $p_{T_{j_3}}$, for the SM signal and the total background. Although the latter has a harder spectrum than the signal, imposing too stringent a veto is not advantageous. This is because the $b\bar{b}b\bar{b}$ final state leads to a non-negligible amount of hadronic activity in the central region, for instance due to gluon radiation from the b quarks and to b -jet misidentification. Based

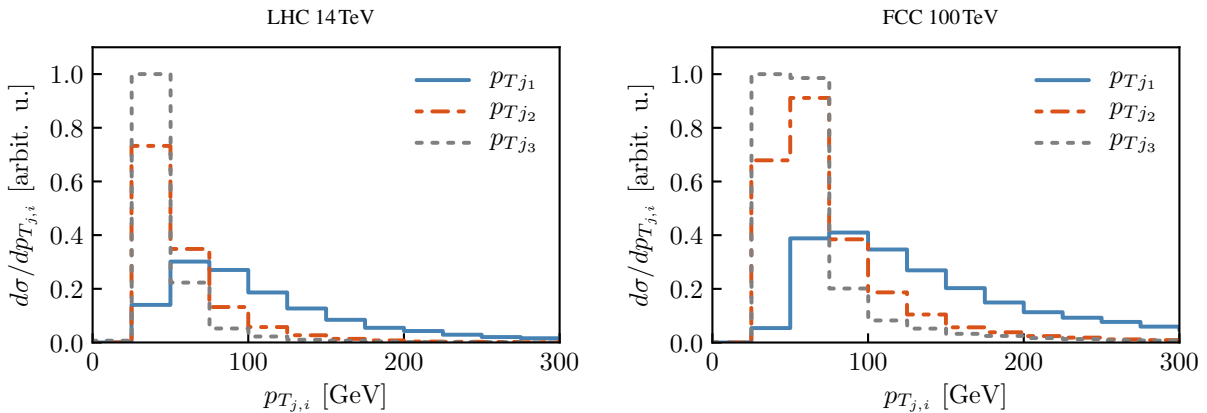


Fig. 5 Distributions of the p_T of the leading, subleading, and 3rd light jet at 14 TeV (left panel) and 100 TeV (right panel) for the SM signal. Distributions are area-normalized as in Fig. 3.

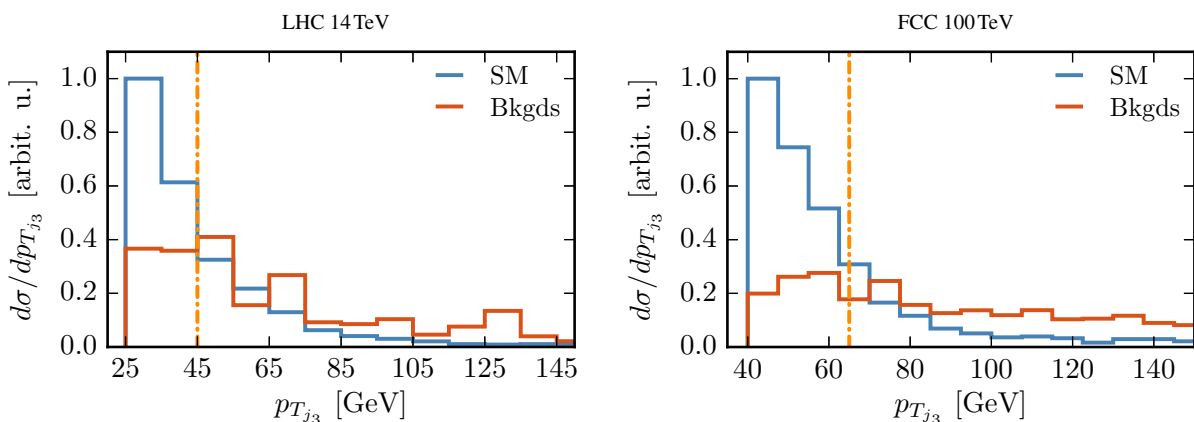


Fig. 6 Distribution of the p_T of the 3rd light jet at 14 TeV (left panel) and 100 TeV (right panel) for the SM signal and the total background, including only events where this jet lies within the pseudo-rapidity region between the VBF jets. The vertical line indicates the CJV cut.

on these results, in our analysis, we impose a CJV with the threshold value reported in Table 2 and shown in the plots by the dot-dashed line.

3.3 Higgs reconstruction

The next step in our analysis is the reconstruction of the Higgs boson candidates. This is done separately for each of the three event categories. In the resolved category, starting with the six hardest b -jets in the event,¹ we reconstruct the first Higgs boson candidate h_1 by identifying it with the pair of b -jets whose invariant mass is closest to the Higgs mass, $m_h = 125$ GeV. Out of the remaining b -jet pairs, the one with an invariant mass closest to m_{h_1} is then assigned to be the second Higgs boson candidate, h_2 . In the case of the intermediate and boosted categories, each of the mass-drop tagged jets is identified with a Higgs candidate. The second Higgs candidate in the intermediate category is then formed by considering the five hardest b -jets in the event and selecting the pair whose mass is closest to m_h .

The invariant mass distributions of the Higgs candidates for the signal (SM and $c_{2V} = 0.8$) and the total background are shown in Fig. 7. The peak around $m_h = 125$ GeV is clearly visible for signal events, especially in the case of h_1 . The smearing of the signal distribution of the second Higgs candidate h_2 arises from out-of-cone radiation effects which reduce the reconstructed mass. It is largest in the SM, while it is reduced in the $c_{2V} = 0.8$ scenario and in particular at 100 TeV, due to the larger boost of the Higgs bosons. The small peak in the background distributions for h_1 is artificially sculpted by the analysis selection cuts. The fact that the efficiency for the reconstruction of the Higgs bosons is similar

¹Note that we start with the 6 hardest b -jets since gluon splitting generates additional b -jets. Thus, there is a non zero probability of missing signal b -jets (i.e. from Higgs decays) if we only restrict ourselves to the hardest 4.

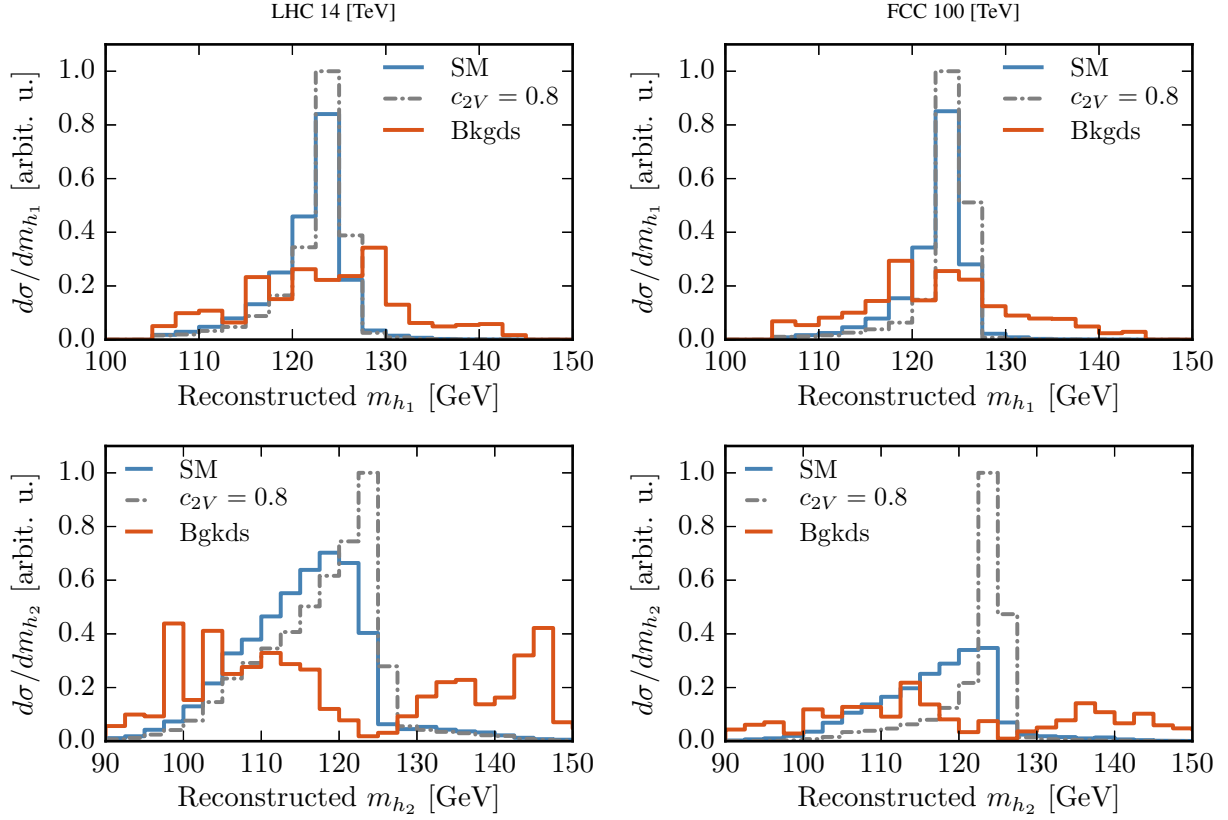


Fig. 7 Invariant mass distribution of the leading (m_{h_1}) and subleading (m_{h_2}) Higgs candidates for signal (SM and $c_{2V} = 0.8$) and background events at 14 TeV (left) and 100 TeV (right).

in the SM and for the $c_{2V} = 0.8$ benchmark is another validation of the scale-invariant tagging, since while in the SM most of the events lead to resolved topologies, the $c_{2V} = 0.8$ scenario is dominated by the boosted category (see Fig. 8 below).

After reconstructing the Higgs candidates, we require that their invariant masses, m_{h_1} and m_{h_2} , are reasonably close to the nominal mass. In the resolved category, these conditions are:

$$|m_{h_1} - 125 \text{ GeV}| \leq 20 \text{ GeV}, \quad (15)$$

$$|m_{h_2} - m_{h_1}| \leq 20 \text{ GeV}. \quad (16)$$

The mass window in Eq. (16) is centered around the mass of the first candidate rather than the nominal Higgs mass in order to make the cut robust against UE and PU effects. For the intermediate and boosted categories, the invariant mass of all Higgs candidates is required to satisfy Eq. (15). The cuts of Eqs. (15)-(16) are especially effective in suppressing the QCD backgrounds which have almost featureless m_{h_i} distributions in the Higgs mass regions. Finally, we impose an additional cut on the invariant mass of the di-Higgs system:

$$\begin{aligned} \text{LHC 14 TeV : } & m_{hh} > 500 \text{ GeV}, \\ \text{FCC 100 TeV : } & m_{hh} > 1000 \text{ GeV}. \end{aligned} \quad (17)$$

This condition greatly reduces the background rates while leaving the interesting kinematic region at large m_{hh} – where deviations from the SM signal mostly appear – unaffected.

Figure 8 shows the m_{hh} distribution, after all the cuts listed in Tables 2 and Eqs. (15)–(17), for signal (SM and $c_{2V} = 0.8$) and the total background at 14 TeV and 100 TeV. In each case, we show both the sum of the three event categories and the individual contributions from resolved and boosted events. The intermediate category, which contributes very little in all cases, is not shown. This comparison helps illustrate the relative weight of the boosted and resolved

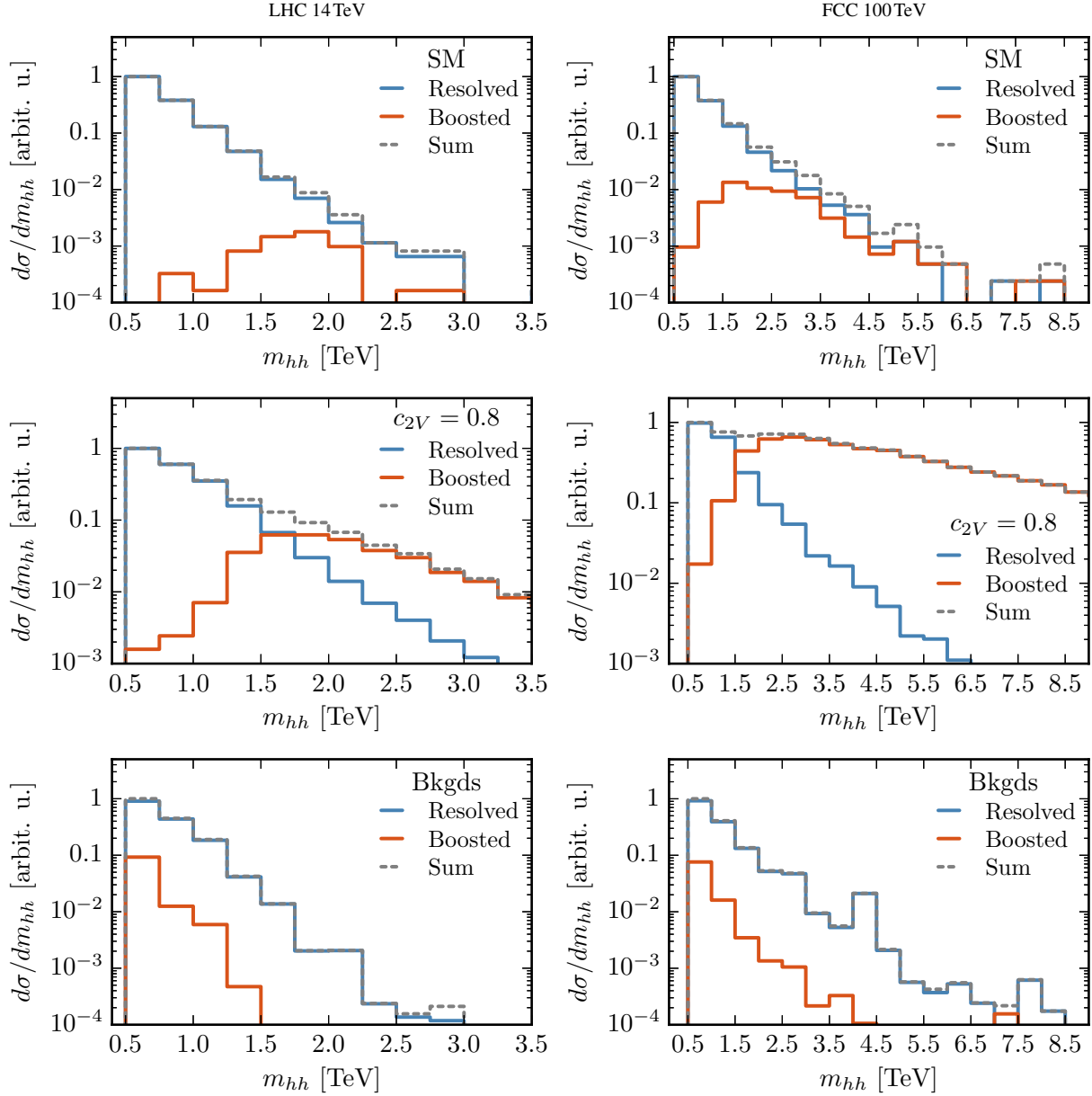


Fig. 8 Invariant mass distribution of the di-Higgs system at 14 TeV (left) and 100 TeV (right) after all analysis cuts, for the signal (SM and $c_{2V} = 0.8$) and the total background. We show the contribution from resolved and boosted events as well as the sum of the three categories.

categories. For signal events in the SM, the vast majority are classified in the resolved category as expected since in this case the boost of the di-Higgs system is small except at 100 TeV and for large m_{hh} values. On the other hand, in the case of $c_{2V} = 0.8$, the energy growth of the partonic cross section induces a much harder m_{hh} spectrum. This implies that, already at 14 TeV, a substantial fraction of events falls in the boosted category which becomes the dominant one at 100 TeV. For $c_{2V} = 0.8$, the crossover between the resolved and boosted categories takes place at $m_{hh} \simeq 1.5$ TeV for both colliders, although this specific value depends on the choice of the jet radius R [10]. Unsurprisingly, background events are always dominated by the resolved topology.

3.4 Signal and background event rates

Now that we have presented our analysis strategy, we can turn to discuss the actual impact on the cross sections and event rates of the various steps of the cut flow. In Table 3 we report the cross sections at 14 TeV and 100 TeV after

acceptance, VBF, Higgs reconstruction, and m_{hh} cuts of Table 2 and Eqs. (15)–(17), respectively, for both the signal (SM and $c_{2V} = 0.8$) and for the total background.

		Cross-sections (fb)			
		Acceptance	VBF	Higgs reco.	m_{hh} cut
14 TeV	Signal SM	0.011	0.0061	0.0039	0.0020
	Signal $c_{2V} = 0.8$	0.035	0.020	0.017	0.011
	Bkgd (total)	1.3×10^5	4.9×10^3	569	47
100 TeV	Signal SM	0.22	0.15	0.11	0.033
	Signal $c_{2V} = 0.8$	3.4	2.7	1.9	1.6
	Bkgd (total)	1.9×10^6	1.9×10^5	9.5×10^3	212

Table 3 Cross sections, in fb, at 14 TeV (upper table) and 100 TeV (lower table) after the successive application of the acceptance and VBF cuts (Table 2) and of the Higgs reconstruction cuts (Eqs. (15)–(17)), for signal events (SM and $c_{2V} = 0.8$) and for the total background.

At 14 TeV, we find that the VBF di-Higgs signal in the SM is rather small already after the basic acceptance cuts. On the other hand, the signal event yield is substantially increased for $c_{2V} \neq 1$ as illustrated by the benchmark value of $c_{2V} = 0.8$ leading to more than a factor 3 (5) enhancement compared to the SM after the acceptance (all analysis) cuts. The fact that this cross-section enhancement for the $c_{2V} = 0.8$ scenario is more marked at the end of the analysis is not a coincidence: our selection cuts have been designed so as to improve the sensitivity to c_{2V} by increasing the signal significance in the large- m_{hh} region.

From Table 3 we also find that a similar qualitative picture holds at 100 TeV with the important difference that, in this case, the event rate is already substantial in the SM which yields $\simeq 2000$ events after the acceptance cuts with $\mathcal{L} = 10 \text{ ab}^{-1}$. The cross section enhancement at 100 TeV as compared to 14 TeV is driven by the larger centre-of-mass energy and leads to a signal rate greater by a factor 20 (17) after the acceptance (all analysis) cuts in the SM, and by a factor $\simeq 100$ (150) in the $c_{2V} = 0.8$ scenario. At 100 TeV, the ratio of signal cross sections in the $c_{2V} = 0.8$ and SM scenarios is ~ 15 (50) after acceptance (all analysis) cuts. Note however that at both 14 TeV and 100 TeV, even after all analysis cuts the background is still much larger than the signal (either SM or $c_{2V} = 0.8$) at the level of inclusive rates. It is only by exploiting the large- m_{hh} region that the former can be made small enough to achieve high signal significances.

Table 3 is also useful to assess the relative impact on the signal and the total background of each of the cuts imposed. In the case of the VBF cuts, we find that the background is drastically reduced, by more than one order of magnitude, at the cost of a moderate decrease of the signal cross sections. The Higgs mass window requirement is also instrumental to further suppress the backgrounds, especially the QCD multijets which are featureless in m_h , while leaving the signal mostly unaffected. A final reduction of the background, by around another order of magnitude, is achieved through the m_{hh} cut. The relative impact of each cut on signal events is similar in the SM and for $c_{2V} = 0.8$.

Figure 9 graphically illustrates the dependence of the di-Higgs production cross section on the couplings c_{2V} and c_3 . The left panel shows the cross section in SM units as a function of $\delta_{c_{2V}} = c_{2V} - 1$ and $\delta_{c_3} = c_3 - 1$ after applying the acceptance cuts of Table 2 (dashed curves) and after all the analysis cuts (solid curves). The sensitivity on c_{2V} is particularly striking, for example the cross section for $|\delta_{c_{2V}}| \simeq 1$ is enhanced by a factor ~ 50 compared to its SM value after all cuts. This sensitivity is the key ingredient for measuring c_{2V} with good precision, even though the SM cross section itself cannot be extracted with comparable accuracy. In particular, as we will show in Sec. 4, the sensitivity to $\delta_{c_{2V}}$ derives mainly from the tail of the m_{hh} distribution. This observation elucidates the enhancement (suppression) in the sensitivity to $\delta_{c_{2V}}$ (δ_{c_3}) in Fig. 9 after the application of all the cuts which, for instance, remove the threshold region up to $m_{hh} = 500$ (1000) GeV at the LHC(FCC).

The right panel of Fig. 9 shows, instead, the ratio between the VBF di-Higgs cross sections at $\sqrt{s} = 100$ TeV and 14 TeV. Given the larger centre-of-mass energy of the FCC, it is expected that this ratio grows rapidly for $\delta_{c_{2V}} \neq 0$ and, indeed, it can reach values as high as 300 for $\delta_{c_{2V}} \simeq 1$. As will be demonstrated in Sec. 4, this effect allows for much more precise measurements of c_{2V} at the FCC, with uncertainties reduced by a factor 20 as compared to the HL-LHC. The results of Fig. 9 are of course consistent with the findings of Table 3.

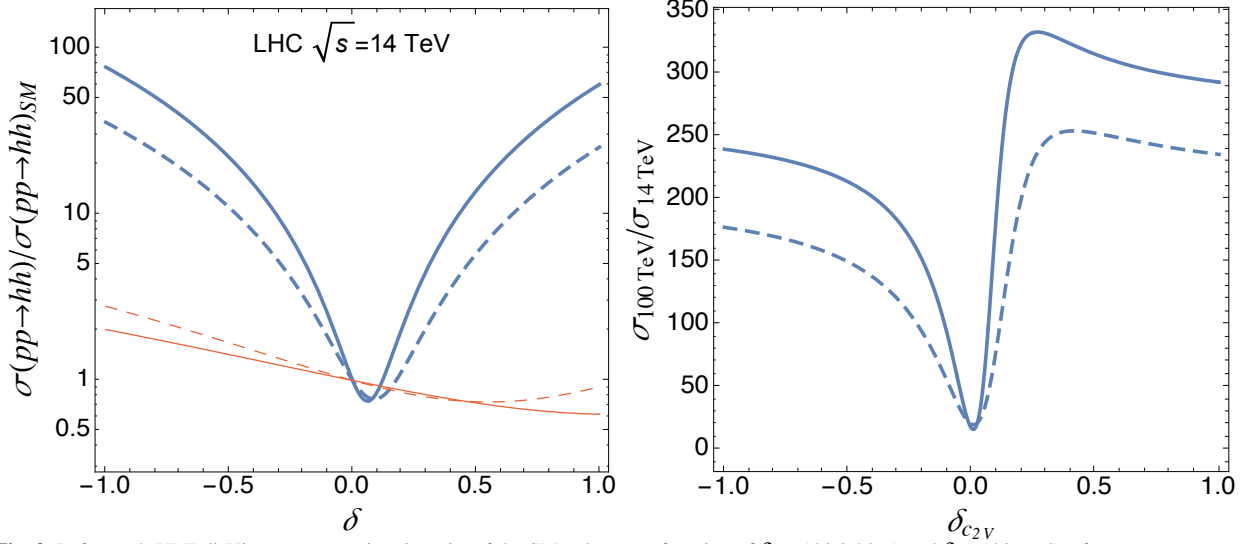


Fig. 9 Left panel: VBF di-Higgs cross-section, in units of the SM value, as a function of $\delta_{c_{2V}}$ (thick blue) and δ_{c_3} (thin red), after acceptance cuts (solid) and all analysis cuts (dashed). Right panel: ratio of VBF di-Higgs cross section between 100 TeV and 14 TeV as a function of $\delta_{c_{2V}}$.

From Fig. 9, we also observe that the sensitivity of the signal on the Higgs trilinear coupling c_3 is relatively weak even for large variations and it is reduced by our analysis strategy. As already mentioned, this latter feature is expected because the sensitivity to c_3 comes from events near the di-Higgs threshold, $m_{hh} \simeq 2m_h$, which are removed by our cuts due to the overwhelming backgrounds in that region. This weak dependence of the VBF di-Higgs cross-section on c_3 , together with the large event rates for background after all the analysis cuts (see Table 3), suggest that the VBF process is not suitable to extract the Higgs self-coupling.

Let us now turn to discuss the background processes. As mentioned above and discussed in Appendix A, there are two types of processes that contribute to the final-state signature under consideration. The first type are QCD processes and in particular multijet and top-quark pair production in association with additional hard radiation. The second is Higgs pair production in the gluon-gluon fusion channel in association with additional jets, where the latter can mimic the VBF topology, as in single-Higgs production.

In the case of QCD multijet processes, it is important to account for the effects of both the $4b$ and the $2b2j$ backgrounds (where we label each process by its matrix-element level content; as explained in Appendix A, additional jets are generated by the parton shower). The latter process can lead to events being classified as signal when light jets are misidentified as b -jets or when a gluon splits into a $b\bar{b}$ pair during the parton shower. Even with a small light jet mistag rate of $\mathcal{O}(1\%)$, it can have a contribution to the total background comparable to or bigger than the $4b$ process. Details on the generation of the QCD backgrounds and on the associated validation tests are presented in Appendix A and Appendix C.

Concerning gluon-fusion Higgs pair production in association with additional hard jets, similarly to single-Higgs VBF production there will be certain configurations that mimic the VBF topology as emphasized, for example, in Ref. [64]. In contrast to the VBF channel, however, the Higgs pair production in gluon-fusion does not exhibit any enhancement in the tail of the m_{hh} distribution. This substantially reduces its contamination to the region with the highest sensitivity to c_{2V} in our analysis. Note also that a harder m_{hh} distribution could be generated by higher-order EFT operators, for instance those leading to a contact interaction of the form $gghh$, as in Ref. [17]. The investigation of this scenario is however left for future work.

In Table 4, following the structure of Table 3, we give the cross sections at 14 TeV and 100 TeV for the individual background processes (and their sum) after the acceptance, VBF, Higgs reconstruction, and m_{hh} cuts. We find that in all steps in the cut-flow the dominant background component is QCD multijet production, both at 14 TeV and at 100 TeV. After all analysis cuts, the $2b2j$ component is a factor 10 larger than $4b$ at 14 TeV while they are of similar size at 100 TeV.

Other backgrounds, including gluon-fusion di-Higgs production, are much smaller than QCD multijets. Note however that the former is actually larger than the VBF signal for SM couplings with a cross-section at 14 TeV of 0.98 (0.009) fb after acceptance (all) cuts, compared to 0.11 (0.002) fb for the VBF case. On the other hand, this fact

		Acceptance	VBF	Higgs reco.	m_{hh} cut
LHC 14 TeV	$4b$	1.18×10^4	613	54	4.45
	$2b2j$	1.14×10^5	4.31×10^3	514	42.6
	$t\bar{t}jj$	150	4.75	0.732	0.0706
	$gg \rightarrow hh$	0.98	0.0388	0.0223	0.00857
	Total	1.3×10^5	4.9×10^3	569	47
FCC 100 TeV	$4b$	3.93×10^5	4.59×10^4	2.61×10^3	106
	$2b2j$	1.52×10^6	1.46×10^5	6.88×10^3	104
	$t\bar{t}jj$	9.76×10^3	832	55	1.47
	$gg \rightarrow hh$	24.8	2.48	1.31	0.0892
	Total	1.9×10^6	1.9×10^5	9.5×10^3	212

Table 4 Same as Table 3, now listing separately each background process.

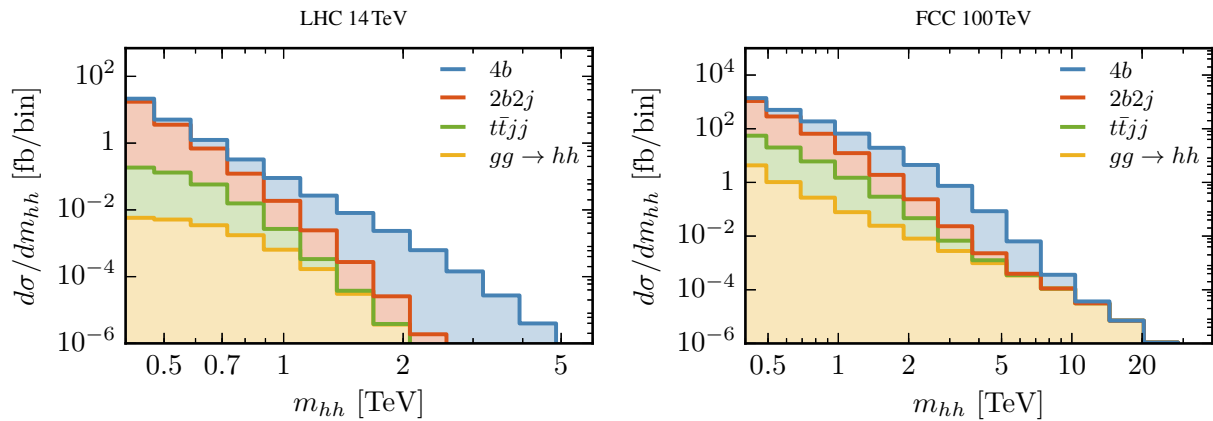


Fig. 10 Decomposition of the total background into individual processes as a function of the di-Higgs invariant mass after all analysis cuts have been imposed, except for the m_{hh} cut.

does not affect the measurement c_{2V} since, as we show next, the sensitivity comes from the large m_{hh} tail where the gluon-fusion component is heavily suppressed.

The decomposition of the total background in terms of individual processes as a function of m_{hh} is shown in Fig. 10 where the components are stacked on top of each other so that the content of each bin matches the total background cross section. In the 14 TeV case, the $4b$ background dominates for large m_{hh} while the $2b2j$ one is instead the most important for small m_{hh} . The 100 TeV case is similar with one exception, namely that the gluon fusion di-Higgs background becomes the dominant one for very high invariant masses, $m_{hh} \gtrsim 10$ TeV. Such extreme region is however phenomenologically irrelevant due to the very small rates of both signal and background even at a 100 TeV collider.

4 Results

The last column of Table 3 indicates the cross sections for the signal and total background after imposing all analysis cuts. We observe that the background, dominated by QCD multijets, still has a much larger cross section than the signal, both in the SM and in the $c_{2V} = 0.8$ benchmark scenario. As anticipated, the additional handle which we can now exploit to increase the signal significance is the different behaviour of the m_{hh} distribution for the signal and the background, in particular when c_{2V} departs from its SM value. The latter has a sharp fall-off at large m_{hh} values while, instead, the signal exhibits a much harder spectrum for $c_{2V} \neq 1$. This cross-section growth implies that, for $|\delta_{c_{2V}}|$ sufficiently large, there will be a crossover value of m_{hh} where the signal overcomes the background.

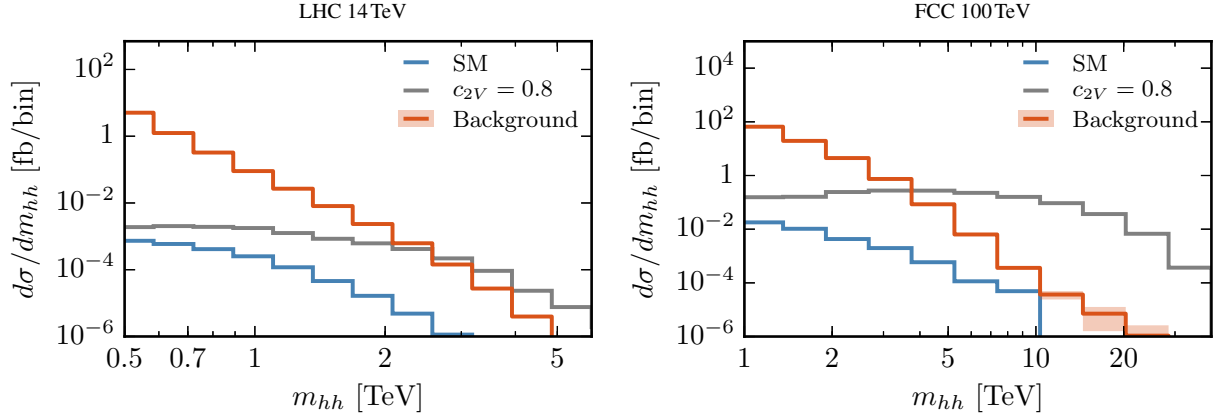


Fig. 11 The di-Higgs m_{hh} distribution at 14 TeV (left) and 100 TeV (right) after all analysis cuts showing the results for the signal (SM and $c_{2V} = 0.8$) and for the total background.

This behaviour is illustrated in Fig. 11 where we show the invariant mass distribution of the Higgs pairs after all analysis cuts, at 14 TeV and 100 TeV, for the signal (SM and $c_{2V} = 0.8$) and the total background. In the case of the benchmark scenario with $c_{2V} = 0.8$, the crossover between signal and background is located at $m_{hh} \simeq 2$ TeV (4 TeV) at 14 TeV (100 TeV). We also observe that, for invariant masses m_{hh} above this crossover, the ratio between the signal and the backgrounds keeps increasing steeply.

With the final results of our analysis in hand, we can now estimate the expected sensitivity to deviations in the $hhVV$ coupling, parametrized as $\delta_{c_{2V}} = c_{2V} - 1$, by exploiting the information contained in the full m_{hh} differential distribution (as opposed to using only the total number of events satisfying all cuts from Table 3). To achieve this, we first bin our results in m_{hh} and then follow a Bayesian approach [109] to construct a posterior probability density function. We include two nuisance parameters, θ_B and θ_S , to account for the uncertainty associated with the background and signal event rate, respectively. The parameter θ_S encodes the theoretical uncertainties on the di-Higgs cross section and the branching fraction $\text{BR}(h \rightarrow b\bar{b})$. We conservatively assume a 10% uncertainty uncorrelated in each m_{hh} bin.

Concerning θ_B , we expect that an actual experimental analysis of di-Higgs production via VBF would estimate the overall normalization of the different background components by means of data-driven techniques. We assume a 15% uncertainty arising from the measurement and subsequent extrapolation of the dominant QCD multijet background, see for example a recent ATLAS measurement of dijet $b\bar{b}$ cross-sections [110]. The background nuisance parameter, θ_B , is conservatively also assumed to be uncorrelated among m_{hh} bins. In addition, while we already rescale the background cross sections to match existing NLO and NNLO results (see Appendix A), there still remains a sizable uncertainty in their overall normalization from missing higher orders, in particular for the QCD multijet components. For this reason, below, we explore the robustness of our results upon an overall rescaling of all the background cross sections by a fixed factor.

The posterior probability function constructed in this way reads:

$$P(\delta_{c_{2V}} | \{N_{\text{obs}}^i\}) = \int \prod_{i \in \{\text{bins}\}} d\theta_S^i d\theta_B^i L(N^i(\theta_B^i, \theta_S^i) | N_{\text{obs}}^i) e^{-(\theta_S^i)^2/2} e^{-(\theta_B^i)^2/2} \pi(c_{2V}), \quad (18)$$

with $N^i(\theta_B^i, \theta_S^i)$ and N_{obs}^i denoting respectively the number of predicted (for a generic value of c_{2V}) and observed (assuming SM couplings) events for a given integrated luminosity \mathcal{L} in the i -th bin of the di-Higgs invariant mass distribution m_{hh} , given by ²:

$$N^i(\theta_B, \theta_S) = \left[\sigma_{\text{sig}}^i(c_{2V}) (1 + \theta_S^i \delta_S) + \sigma_{\text{bkg}}^i (1 + \theta_B^i \delta_B) \right] \times \mathcal{L}, \quad (19)$$

$$N_{\text{obs}}^i = \left[\sigma_{\text{sig}}^i(c_{2V} = 1) + \sigma_{\text{bkg}}^i \right] \times \mathcal{L}.$$

In Eq. (19), $\sigma_{\text{sig}}^i(c_{2V})$ and σ_{bkg}^i indicate the signal (for a given value of c_{2V}) and total background cross sections, respectively, for the i -th bin of the m_{hh} distribution. The functional form of $\sigma_{\text{sig}}^i(c_{2V})$ is given by Eq. (7) and the value

²In our analysis, we use 15 bins starting at 250 GeV up to 6(30)TeV for the LHC(FCC) that are uniformly spaced on a log scale. In addition, we define an overflow bin up to the relevant centre of mass energy.

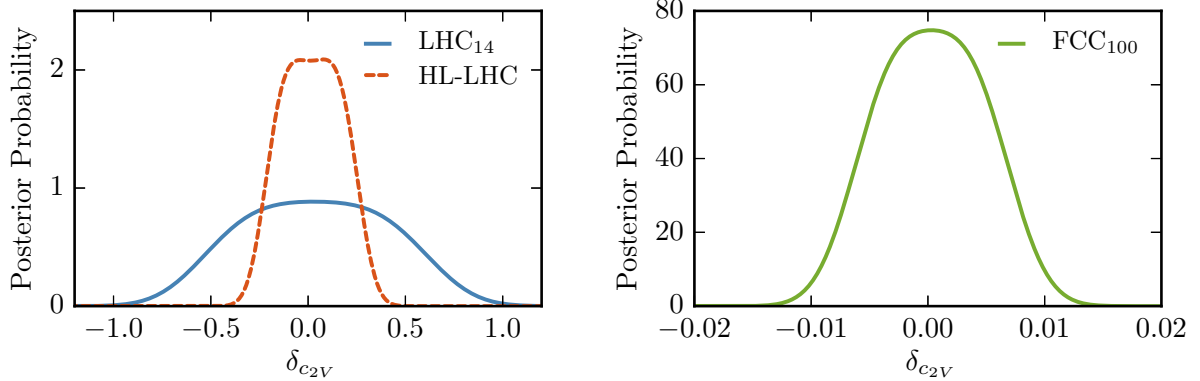


Fig. 12 Posterior probability densities for $\delta_{c_{2V}}$ at the LHC for $\mathcal{L} = 300 \text{ fb}^{-1}$ (LHC₁₄) and $\mathcal{L} = 3 \text{ ab}^{-1}$ (HL-LHC) and for the FCC with $\mathcal{L} = 10 \text{ ab}^{-1}$. Note the different scales of the axes in the two panels.

	68% probability interval on $\delta_{c_{2V}}$	
	$1 \times \sigma_{\text{bkg}}$	$3 \times \sigma_{\text{bkg}}$
LHC ₁₄	[-0.37, 0.45]	[-0.43, 0.48]
HL-LHC	[-0.15, 0.19]	[-0.18, 0.20]
FCC ₁₀₀	[0, 0.01]	[-0.01, 0.01]

Table 5 Expected precision (at 68% probability level) for the measurement of $\delta_{c_{2V}}$ at the LHC and the FCC, assuming SM values of the Higgs couplings. We show results both for the nominal background cross section σ_{bkg} , and for the case in which this value is rescaled by a factor 3.

of the coefficients in bin i are given in Appendix D. We denote by $\pi(c_{2V})$ the prior probability distribution of the c_{2V} coupling.

As justified above, in the evaluation of Eq. (18) we set $\delta_{B(S)} = 0.15$ (0.1) and assume that the two nuisance parameters are normally distributed. We have verified that assuming instead a log normal distribution leads to similar results. In addition, we take a Poissonian likelihood $L(N^i | N_{\text{obs}}^i)$ in each bin and assume the prior probability $\pi(c_{2V})$ to be uniform. The resulting posterior probabilities are shown in Fig. 12 for the LHC with $\mathcal{L} = 300 \text{ fb}^{-1}$ (LHC₁₄) and $\mathcal{L} = 3 \text{ ab}^{-1}$ (HL-LHC), and for the FCC with $\mathcal{L} = 10 \text{ ab}^{-1}$. To produce this figure, as well as to determine the values reported in Tabs. 5 and 6, we included all bins with at least one event.

From Fig. 12, we can determine the expected precision for a measurement of $\delta_{c_{2V}}$ at the LHC and the FCC in the case of SM values of the Higgs couplings. The 68% probability intervals for the determination of c_{2V} at the LHC and the FCC are listed in Table 5. This is the central result of this work. To assess its robustness with respect to our estimate of the background cross sections, we also provide the same intervals in the case of an overall rescaling of the total background by a factor 3. Furthermore, we can also assess the effect of varying c_V on the bound on $\delta_{c_{2V}}$ by treating c_V as a nuisance parameter and marginalizing over it. The leading effect of varying c_V comes from the $(c_{2V} - c_V^2)$ term at the amplitude level – see Eq. 4 – and can be included using the parametrization of Eq. 8. The neglected dependence is sub-leading and arises from the interference of diagrams proportional to c_V^2 and $c_V c_3$. We take c_V to be Gaussian distributed with a mean equal to 1 (i.e., its SM value) and a width equal to 4.3%, 3.3%, and 2% at the LHC Run II, HL-LHC, and FCC respectively. In case of the LHC (both Run II and HL), the width of the Gaussian corresponds to the projected sensitivity from the two parameter fit by ATLAS [111]. The effect of marginalizing over c_V is sub-leading in both LHC scenarios and weakens the bound on $\delta_{c_{2V}}$. We find that the results of Table 5 change by 2% for LHC₁₄ and 7% for HL-LHC. The effect at the FCC is much larger causing the bound on $\delta_{c_{2V}}$ to be $\mathcal{O}(0.04)$ rather than 0.01. This is not surprising and indicates that a joint likelihood would be required at the FCC.

From Table 5, we find that the c_{2V} coupling, for which there are currently no direct experimental constraints, can already be measured at the LHC with 300 fb^{-1} with a reasonably good accuracy: $^{+45\%}_{-37\%}$ with 68% probability. This accuracy is only marginally degraded if the background is increased by a factor 3. A better precision, of the order of $^{+19\%}_{-15\%}$, is expected at the HL-LHC with 3 ab^{-1} . Also, this estimate is robust against an overall rescaling of the background cross section. Finally, we find a very significant improvement at the FCC with 10 ab^{-1} , where a measurement at the 1% level could be achieved providing an unprecedented test for our understanding of the Higgs sector.

	95% probability upper limit on μ	
	$1 \times \sigma_{\text{bkg}}$	$3 \times \sigma_{\text{bkg}}$
LHC ₁₄	109	210
HL-LHC	49	108
FCC ₁₀₀	12	23

Table 6 95% probability upper limits on the fiducial signal strength, $\mu = \sigma/\sigma_{\text{SM}}$.

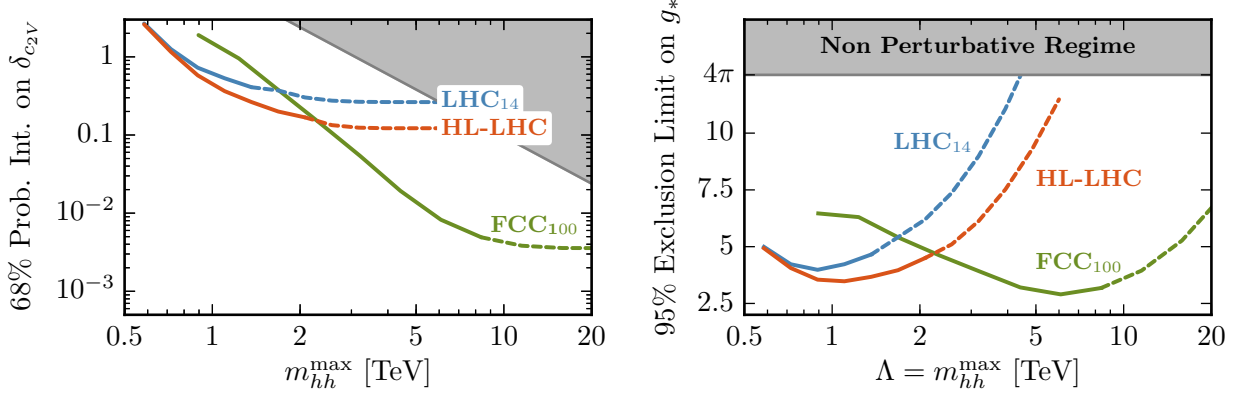


Fig. 13 Left: the expected precision for a measurement of $\delta_{c_{2V}}$ at the 68% CL as a function of m_{hh}^{max} for the LHC and the FCC. The gray area indicates the region where $\delta_{c_{2V}} > \delta_{c_{2V}}^{\text{max}}$, obtained by setting $\Lambda = m_{hh}^{\text{max}}$. Right: the 95% CL exclusion limits in the $(\Lambda = m_{hh}, g_*)$ plane, assuming Eq. (20), where again the gray area corresponds to the non-perturbative regime, defined by $g_* \geq 4\pi$. The transition between solid and dashed curves occurs at the last bin with at least one event.

It is interesting to compare these results with the experimental precision expected on the fiducial VBF di-Higgs production cross section after all analysis cuts, expressed in terms of the signal strength parameter normalized to the SM result, $\mu = \sigma/\sigma_{\text{SM}}$. Table 6 shows the 95% upper limits on μ for the nominal background cross section and after rescaling the latter by a factor 3. The comparison with Table 5 clearly shows that the high precision expected on c_{2V} can be obtained despite the rather loose constraints that can be obtained on the VBF di-Higgs cross section even at 100 TeV. As already discussed, this behaviour follows from the strong dependence of the signal cross section on c_{2V} , see Fig. 9.

The results of Tables 5 and 6 have been obtained by making full use of the information contained on the di-Higgs invariant mass distribution m_{hh} . However, the EFT expansion might break down at large enough values of m_{hh} , corresponding to large partonic center-of-mass energies, and some assessment on the validity of our procedure is thus required. In particular, results can be consistently derived within the EFT framework only if the new physics scale Λ is smaller than the largest value of m_{hh} included in the analysis.

As stressed in Ref. [97], constraining Λ requires making assumptions on the structure of the UV dynamics extending the SM. For example, for the case where the new physics is characterized by a single coupling strength g_* and mass scale Λ [3], one naively expects

$$\delta_{c_{2V}} \approx g_*^2 v^2 / \Lambda^2. \quad (20)$$

Therefore, for maximally strongly-coupled UV completions (with $g_* \simeq 4\pi$) it is possible to derive the following upper limit,

$$\delta_{c_{2V}}^{\text{max}} \approx 16\pi^2 v^2 / \Lambda^2, \quad (21)$$

which makes explicit the connection between the value of $\delta_{c_{2V}}$ and the new physics scale Λ . The validity of the EFT can thus be monitored by introducing a restriction on the m_{hh} bins used in the construction of the posterior probability Eq. (18), so that $m_{hh} \leq m_{hh}^{\text{max}}$, and then determining how the sensitivity on $\delta_{c_{2V}}$ varies as a function of m_{hh}^{max} [97].

The precision on $\delta_{c_{2V}}$, defined through the symmetrized 68% probability interval, is shown in Fig. 13 as a function of m_{hh}^{max} for the LHC and the FCC. As expected, increasing m_{hh}^{max} , *i.e.* making the cut less stringent, leads to stronger constraints. Eventually, $\delta_{c_{2V}}$ flattens out when m_{hh}^{max} is large enough that all the m_{hh} bins which contain at least one event are included in the posterior probability of Eq. (18). Bins which contain at least one event are depicted in Fig. 13 with a solid curve, while those containing less than one event are depicted by a dashed curve. The gray area in Fig. 13

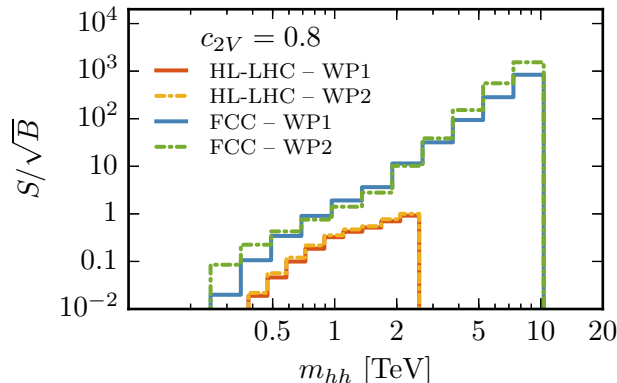


Fig. 14 Signal significance S/\sqrt{B} in the $c_{2V} = 0.8$ scenario, as a function of the di-Higgs invariant mass m_{hh} at the HL-LHC and the FCC, for the two b -tagging working points of Eq. (13).

corresponds to the non-perturbative region where $\delta_{c_{2V}} > \delta_{c_{2V}}^{\max}$, obtained by setting $\Lambda = m_{hh}^{\max}$ in Eq. (21), the most optimistic assumption compatible with the validity of the EFT expansion.

As an additional way to quantify the validity of the EFT approach in our analysis, we derive the region of exclusion in the plane (Λ, g_*) [97], corresponding to the limits on $\delta_{c_{2V}}$ derived as a function of m_{hh}^{\max} . This is shown in the left panel of Fig. 13, making use of Eq. (20) and then setting $\Lambda = m_{hh}^{\max}$. The gray area in the upper part of the plot indicates the non-perturbative region, defined by $g_* \geq 4\pi$. We find that the dominant constraints on $\delta_{c_{2V}}$ arise from a region in the parameter space where the EFT expansion is valid, both at the LHC and at the FCC. The results from the two panels of Fig. 13 indicate that our EFT analysis is robust and that can be used to derive stringent bounds on $\delta_{c_{2V}}$ in the absence of new explicit degrees of freedom.

Finally, in Fig. 14 we show the signal significance, S/\sqrt{B} , in the $c_{2V} = 0.8$ scenario as a function of the di-Higgs invariant mass m_{hh} at the HL-LHC and the FCC. The results are presented for the two b -tagging working points defined in Eq. (13). As already discussed, these have been chosen so that the first (WP1) is consistent with the current ATLAS and CMS performances, while the second (WP2) assumes an improved detector performance. One can observe that the signal significance of each individual bin is at most $S/\sqrt{B} \simeq 2$ at the HL-LHC (though the precise numbers depend on the specific choice of binning), while at the FCC one finds much higher signal significances, with $S/\sqrt{B} \simeq 5$ already for $m_{hh} \simeq 1.5$ TeV and then increasing very rapidly for higher values of m_{hh} . Figure 14 clearly shows that the signal significance depends very mildly on the specific details of the b -tagging performance and that operating at WP2 instead of WP1 implies only a minor improvement.

To summarize, we have demonstrated how Higgs boson pair production via VBF can be used to provide the first direct constraints on the c_{2V} coupling already at the LHC with $\mathcal{L} = 300 \text{ fb}^{-1}$ (Table 5), which at a 100 TeV collider would become a high-precision measurement with potentially sub-percent accuracy. We have also assessed (Fig. 13) the robustness of our strategy and the validity of the underlying EFT expansion. Our analysis clearly highlights the unique physics potential of extending current di-Higgs searches at the LHC to the vector-boson fusion channel.

5 Conclusions and Outlook

The measurement and study of Higgs pair production is one of the cornerstones of the LHC program as well as of any future hadron collider. It provides unique information on the Higgs sector and on the mechanism underlying electroweak symmetry breaking, and allows a direct test of the strength of the Higgs boson self-interactions. On the other hand, it is a challenging measurement and the low production rates require large integrated luminosities to achieve reasonable signal significances. While most studies of Higgs pair production so far have concentrated on the gluon-fusion channel which has the largest cross section, we have shown in this work how the vector-boson fusion channel can impose stringent constraints on Higgs couplings that are not directly accessible by other means, in particular on the $hhVV$ quartic coupling c_{2V} .

Exploiting the high signal yield of the $b\bar{b}b\bar{b}$ final state, we have presented a detailed feasibility study of the measurement of Higgs boson pairs in the vector-boson fusion channel at the LHC and at a future 100 TeV hadron collider. A key ingredient of our strategy is provided by the fact that deviations of the Higgs couplings to vector bosons from the

parabola $c_{2V} = c_V^2$ significantly harden the m_{hh} distribution resulting in a large fraction of events with a boosted Higgs pair. The subsequent decays into $b\bar{b}$ pairs can then be reconstructed by means of jet substructure techniques. While QCD backgrounds are very large, we have shown how the combination of selection cuts exploiting the VBF topology and the growth of the m_{hh} distribution when the Higgs couplings depart from their SM values leads to a remarkable model-independent sensitivity to the c_{2V} coupling.

Our results demonstrate that at the LHC with an integrated luminosity of $\mathcal{L} = 300$ (3000) fb^{-1} the $hhVV$ coupling can be measured with $^{+45\%}_{-37\%}$ ($^{+19\%}_{-15\%}$) precision at the 68% probability level, reaching 1% accuracy at a 100 TeV collider. Therefore, stringent constraints on this so far unknown coupling can be obtained already before the start of the HL-LHC data taking. Our analysis provides strong motivation for the ATLAS and CMS collaborations to extend their searches for Higgs pair production to the VBF channel already during Runs II and III. On the other hand, we also find that the VBF channel is clearly inferior to the gluon-fusion channel for a measurement of the Higgs self-coupling λ , at least for the $b\bar{b}b\bar{b}$ final state studied here, since the sensitivity to λ arises from the threshold region $m_{hh} \simeq 2m_h$ where QCD backgrounds overwhelm the signal even for sizeable modifications of the Higgs couplings with respect to their SM values.

There are several possible avenues for future work. On one hand, it might be interesting to study the possibility to enhance the sensitivity to c_{2V} by means of a multivariate analysis (MVA), such as those used in [43], in order to dynamically determine the optimal set of selection cuts and optimise the discrimination between signal and background events. Further, it should be possible to quantify the constraints on additional EFT operators that can contribute to the di-Higgs VBF signal yield and that have not been considered in this work. Finally, a complete analysis should include a full detector simulation, especially for the reconstruction of the forward jets and of the Higgs boson candidates, and a b -tagging strategy able to reproduce more closely the one adopted by the LHC experiments.

Acknowledgements

We thank Nathan Hartland for assistance with the Sherpa event generation and for many discussions about Higgs pair production. F. B. is supported a STFC Consolidated Grant and acknowledges the hospitality and support of the CERN Theory department. The work of R. C. was partly supported by the ERC Advanced Grant No. 267985, *Electroweak Symmetry Breaking, Flavour and Dark Matter: One Solution for Three Mysteries (DaMeSyFla)*. J. R. is supported by the ERC Starting Grant ‘‘PDF4BSM’’.

Appendix A: Monte Carlo event generation

In this Appendix we discuss the event generation of the signal and background process used in this analysis. In each case, we discuss the programs used, the input parameters and theoretical settings, and the cross-checks that have been performed.

Signal events for Higgs pair production via VBF have been generated at leading order (LO) with MadGraph5_aMC@NLO [112] using a tailored UFO [113] model that allows for generic values of the c_V , c_{2V} , and c_3 couplings in the Lagrangian Eq. (2) (see [114, 115] for other UFO models of Higgs EFTs). We generated 1M unweighted events for each value of c_{2V} and for center-of-mass energies of 14 TeV and 100 TeV. The size of the signal sample is dictated by the condition of achieving an adequate coverage of the large m_{hh} region. Even so, for small deviations of c_{2V} with respect to its SM value this region is very difficult to populate. We overcome this limitation by performing a fit to the cross-section in each m_{hh} bin as a function of c_{2V} using the general parametrization of Eq. (7).

The MadGraph5_aMC@NLO generation of signal events uses the NNPDF2.3LO [116] set with $\alpha_S(m_Z) = 0.119$ interfaced via LHAPDF6 [117]. The calculation is performed in the $n_f = 4$ scheme and the factorization and renormalization scales are taken to be the W boson mass, $\mu_F = \mu_R = M_W$. To account for higher order effects, we apply an NNLO/LO K -factor $\simeq 1.1$ to the inclusive cross-section [63] both at 14 TeV and at 100 TeV. The decays of the Higgs bosons into $b\bar{b}$ pairs are performed within MadGraph5_aMC@NLO with adjusted parameters to ensure that the branching ratio corresponds to Higgs Cross-Section Working Group value [35] of $\text{BR}(h \rightarrow b\bar{b}) = 0.582$. Since in this work we only modify the c_{2V} coupling, assuming the SM value of the total Higgs width is a very good approximation.

With this setup, we have generated signal events in the SM and for a wide range of values of $\delta_{c_{2V}}$. At the matrix-element level, we applied the generation cuts listed in Table 7. The corresponding cross sections are summarized in Table 8, where we provide the SM results as well as the predictions for various BSM scenarios defined by the couplings

	14 TeV		100 TeV	
	Signal	QCD bkg.	Signal	QCD bkg.
pr_j (GeV) \geq	25	20	25	20
pr_b (GeV) \geq	25	20	25	20
$ \eta_j \leq$	4.5	3	10	3
$ \eta_b \leq$	2.5	3	3	3
$\Delta R_{bb} \geq$	0.1	0.1	0.1	0.1
$\Delta R_{jb} \geq$	0.4	0.1	0.4	0.1
$\Delta R_{jj} \geq$	4	0.1	4	0.1
m_{jj} (GeV) \geq	600	—	600	—

Table 7 Parton-level generation cuts for the VBF di-Higgs signal and the QCD background samples at $\sqrt{s} = 14$ TeV and 100 TeV. In this table, j refers to light quarks and gluons, b to bottom quarks, and m_{jj} is the invariant mass of the two light partons in the event with largest p_T^j .

Signal: VBF $hh \rightarrow b\bar{b}b\bar{b}$					
$\{c_V, c_{2V}, c_3\}$		LHC 14 TeV		FCC 100 TeV	
		σ (fb)	$N_{\text{ev}}(\mathcal{L} = 3 \text{ ab}^{-1})$	σ (fb)	$N_{\text{ev}}(\mathcal{L} = 10 \text{ ab}^{-1})$
{1,1,1}	SM	0.26	780	15	$1.5 \cdot 10^5$
{1,0,1}		4.4	$1.3 \cdot 10^4$	593	$5.9 \cdot 10^6$
{1,2,1}		2.5	$7.5 \cdot 10^3$	471	$4.7 \cdot 10^6$
{1,0,0}		5.8	$1.7 \cdot 10^4$	656	$6.6 \cdot 10^6$
{1,0,-1}		7.5	$2.3 \cdot 10^4$	731	$7.3 \cdot 10^6$
{1,1,0}		0.64	$1.9 \cdot 10^3$	30	$3.0 \cdot 10^5$
{1,0.8,1}	Benchmark	0.58	1740	48	$4.8 \cdot 10^5$

Table 8 Parton-level cross sections for VBF Higgs pair production in the $b\bar{b}b\bar{b}$ final state at 14 TeV and 100 TeV (including branching ratios) after the acceptance cuts of Table 7. We show the cross-sections for different values of the couplings $\{c_V, c_{2V}, c_3\}$ normalized to the SM values. We also provide the number of events at the HL-LHC for $\mathcal{L} = 3 \text{ ab}^{-1}$ and at the FCC for $\mathcal{L} = 10 \text{ ab}^{-1}$.

$\{c_V, c_{2V}, c_3\}$, including the benchmark scenario $c_{2V} = 0.8$. In addition, the number of expected events at the HL-LHC, assuming an integrated luminosity of $\mathcal{L} = 3 \text{ ab}^{-1}$, and at the FCC 100 TeV for $\mathcal{L} = 10 \text{ ab}^{-1}$, are also listed.

Following the parton-level event generation, the resulting Les Houches event files for signal events are showered using the Pythia8 Monte Carlo generator [118] v8.212 using the Monash 2013 Tune [119]. No hadronization or underlying event (UE) effects are included for simplicity. Although we have not attempted to simulate the effects of pile-up (PU) in our analysis, recent studies [43] indicate that modern PU mitigation techniques [120] should be efficient enough to minimize the PU contamination even for the $b\bar{b}b\bar{b}$ final state.

Concerning the generation of the QCD background processes, their parton-level cross sections are summarized in Table 9. In each case, we indicate the programs used for the event generation, the number of MC events N_{ev} that have been generated, whether the events are weighted or unweighted, and the LO cross sections along with the corresponding higher-order K -factors at 14 TeV and 100 TeV. As discussed in Sec. 4, our results include a 15% systematic uncertainty on the total background normalization (assuming a data-driven determination in an experimental analysis), and we also assessed the robustness of our estimate for the measurement of $\delta_{c_{2V}}$ in case of an overall upwards shift of the backgrounds by a factor 3.

For QCD multijet production we have explored two complementary approaches for event generation. First of all, we used ALPGEN [121] to generate a large sample of unweighted events at the matrix-element level and showered them with Pythia8. This approach, however, presents a difficulty, because the differential cross section with respect to the di-Higgs invariant mass m_{hh} falls very rapidly for increasing m_{hh} . We thus find that an unrealistically large sample of unweighted events would be needed in order to adequately populate the tail of the m_{hh} distribution.

To bypass this limitation, we generated 50M weighted $4b$ and $2b2j$ events with Sherpa v2.2 [123] and then processed them with the built-in shower. The main advantage of this approach is that events with small weights are not discarded by the unweighting and, therefore, enough events with large m_{hh} (and thus small weight) are still kept. One

Background processes							
Process	Program	N_{ev}	σ_{LO} (fb)		K -factor		Ref.
			LHC14	FCC100	LHC14	FCC100	
$4b$	Sherpa2.2	50M [W]	$1.1 \cdot 10^6$	$1.6 \cdot 10^7$	1.7	1.7	[112]
$2b2j$	Sherpa2.2	50M [W]	$2.6 \cdot 10^8$	$3.8 \cdot 10^9$	1.3	1.3	[112]
$t\bar{t}jj$	Sherpa2.2	10M [W]	$1.9 \cdot 10^4$	$1.6 \cdot 10^6$	1.6	1.6	[122]
$4b2j$	ALPGEN	6M(2M) [UW]	$5.4 \cdot 10^4$	$2.4 \cdot 10^6$	1.7	1.7	–
$2b4j$	ALPGEN	260k [UW]	10^7	$5.2 \cdot 10^8$	1.3	1.3	–
$gg \rightarrow hh \rightarrow b\bar{b}b\bar{b}$	aMC@NLO	1M [UW]	6.2	272	2.4	2.2	[47]

Table 9 Parton level cross-sections for the background processes considered in this work after the acceptance cuts of Table 7. We indicate the programs used, the numbers of events generated N_{ev} and whether they are weighted [W] or unweighted [UW], the LO cross sections and the corresponding K -factors and the relevant reference. In the case of the $4b2j$ and $2b4j$ backgrounds, the same K -factors as those for the $4b$ and $2b2j$, respectively, were applied. For the $4b2j$ sample, the 6M(2M) events correspond to those generated at the LHC(FCC) centre of mass energies, respectively. The generation cuts used for the ALPGEN samples are different, see text.

possible drawback is that, for the same number of events, the unweighted sample provides a better estimate of the total cross section than the weighted one. In our case this is not an issue, since with our weighted sample we achieve statistical uncertainties of order 2% (to be compared with $\gtrsim 0.01\%$ for a same-size unweighted sample), which is more than sufficient for our purposes. On the other hand, to generate a large enough number of events in a reasonable amount of CPU time we are forced to use a lower multiplicity final state, and thus we rely on the parton shower to generate the additional light partons (see Table 9). To validate this procedure, we explicitly verified that, in the region where the two approaches lead to sufficient statistics, the Sherpa calculation based on $4b$ ($2b2j$) matrix elements and the ALPGEN one, based on $4b2j$ ($2b4j$) matrix elements, lead to comparable results (see Appendix C). This agreement indicates that the parton shower does a reasonable job in modelling additional hard radiation in the phase-space region of interest.

The Sherpa samples in Table 9 have been generated using the NNPDF3.0 NNLO set [124] with strong coupling $\alpha_S(m_Z^2) = 0.118$ and with $n_f = 4$ active quark flavours, and use as factorization and renormalization scales $\mu_F = \mu_R = H_T/2$, with

$$H_T \equiv \sum_i^n \sqrt{(m_{t,i})^2 + (p_{T,i}^t)^2}, \quad (\text{A.1})$$

where n is the final-state matrix-element multiplicity and $m_{t,i}$ and $p_{T,i}^t$ are the transverse mass and transverse momentum of the i -th final-state parton. The generation-level acceptance cuts applied to these samples are listed in Table 7. As for the other background samples, LO cross sections have been rescaled by the best available higher-order K -factors.

Higgs pair production via gluon-fusion is simulated at LO using MadGraph5_aMC@NLO for loop-induced processes [125]. The cross-section is rescaled to match the inclusive NNLO+NNLL calculation [47] yielding a K -factor, $\sigma_{\text{NNLO+NNLL}}/\sigma_{\text{LO}} = 2.4$ (2.2) at 14TeV (100TeV). Parton-level events are then showered with Pythia8 using the same settings as for the signal VBF di-Higgs samples. No generation cuts are applied, and the resulting cross sections (including the branching fraction into $b\bar{b}b\bar{b}$) are listed in Table 9. While the hard-scattering process that is generated, $gg \rightarrow hh$, does not include additional jets, initial state radiation from the gluon legs can give a VBF-like topology with two forward jets characterized by a large invariant mass, and thus contribute to the total $hhjj$ yield. We have verified that our calculation provides a reasonable description of the relevant kinematical distributions, such as m_{hh} , by comparing with the $gg \rightarrow hhjj$ process computed in the EFT approximation. As shown in Sec. 4, while the gluon-fusion contamination to the VBF signal is substantial close to threshold, it is marginal in the large m_{hh} region where the sensitivity to c_{2V} is the highest.

Appendix B: Fitting the tail of the m_{hh} distribution for background processes

The background processes considered in this work (see Appendix A) exhibit a steep fall-off for large values of m_{hh} , the invariant mass distribution of the reconstructed Higgs pair. Even with the use of weighted events, it is difficult to adequately populate this region. To obtain a reliable estimate of the cross section there, it is thus necessary to introduce

\sqrt{s} [TeV]	Background	a	b	c
14	$4b$	14.2	0.492	0.512
	$2b2j$	24.9	-2.65	0.198
	$t\bar{t}jj$	48	-18.3	-3.63
	ggf	30.1	-8.27	-1.82
100	$4b$	32.3	-4.82	-0.539
	$2b2j$	36.8	-2.97	-0.118
	$t\bar{t}jj$	38.4	-3.31	-0.265
	$gg \rightarrow hh$	15.9	3.61	0.695

Table 10 The fit coefficients in Eq. (B.2) for each background process at 14 TeV and 100 TeV.

a fitting procedure. In this Appendix we discuss how the fits to the m_{hh} distributions for the background processes, and the associated validation tests, have been performed.

We found that, far from the di-Higgs production threshold, the following functional form provides a reasonable description of the m_{hh} distribution:

$$\sigma^{(\text{fit})}(m_{hh}, \sqrt{s}) = \left[1 - \left(\frac{m_{hh}}{\sqrt{s}} \right)^{1/4} \right]^a \left(\frac{m_{hh}}{\sqrt{s}} \right)^{b+c \cdot \log(m_{hh}/\sqrt{s})}, \quad (\text{B.2})$$

where \sqrt{s} is the collider centre-of-mass energy. This specific functional form is a modified version of one of those suggested in Ref. [126] for the fit of the di-photon invariant mass distribution at the LHC. We explored other choices, finding a comparable fit quality.

In Eq. (B.2), the fit parameters $\{a, b, c\}$ are determined by minimizing the χ^2 ,

$$\chi^2 = \sum_{i=1}^n \frac{\left(\sigma_i^{(\text{th})} - \sigma^{(\text{fit})}(m_{hh}^{(i)}, \sqrt{s}) \right)^2}{\delta_i^2}, \quad (\text{B.3})$$

where n is the number of bins in the m_{hh} distribution used as input to the fit, $\sigma_i^{(\text{th})}$ is the theoretical prediction for the cross-section in the bin $m_{hh}^{(i)}$, and

$$\delta_i \equiv \sqrt{\sum_{k=1}^{N_i} \left(w_k^{(i)} \right)^2}, \quad (\text{B.4})$$

is the statistical uncertainty associated to the N_i weighted Monte Carlo events that populate bin i with weights $\{w_k^{(i)}\}$. Note that when the MC events are unweighted, $\delta_i \propto \sqrt{N_i}$, as expected. The resulting fit coefficients are shown in Table 10 for both centre-of-mass energies and for the four background processes considered. We have also verified that the results for the fit parameters are stable with respect to variations of the binning in m_{hh} .

To validate the fitting procedure, we show in Fig. 15 the m_{hh} distribution of the reconstructed di-Higgs system for the total background, where each individual process has been fitted separately and then added up to construct the solid histograms. The fit results are compared to the cross-sections from the Monte Carlo generation (indicated by filled circles) with their corresponding statistical uncertainty, Eq. (B.4). In the lower panels of Fig. 15 we show the fit residuals, defined as the difference between MC and fit divided by the statistical uncertainty in each bin. The fact that the parametrized fit agrees with the MC calculations at the 2- σ level or better (in units of the uncertainty of the latter) for a wide range of m_{hh} demonstrate the goodness of these fits.

Note that, in the case of the QCD multijet backgrounds, we exclude the first bin to ensure that the fit is not affected by artificial features in the m_{hh} distribution induced by the analysis selection cuts. Furthermore, in the case of the gluon fusion di-Higgs background, it is necessary to exclude the first few bins of the m_{hh} distribution from the fit. The reason is that in this case there is a production threshold at $2m_h$, and, as a result, the distribution does not decrease monotonically with m_{hh} unless one is far enough from threshold. By excluding these bins, we avoid biasing the resulting fit in the tail of the m_{hh} distribution, the region where a functional form such as Eq. (B.2) does provide an equally satisfactory description as for the rest of background processes.

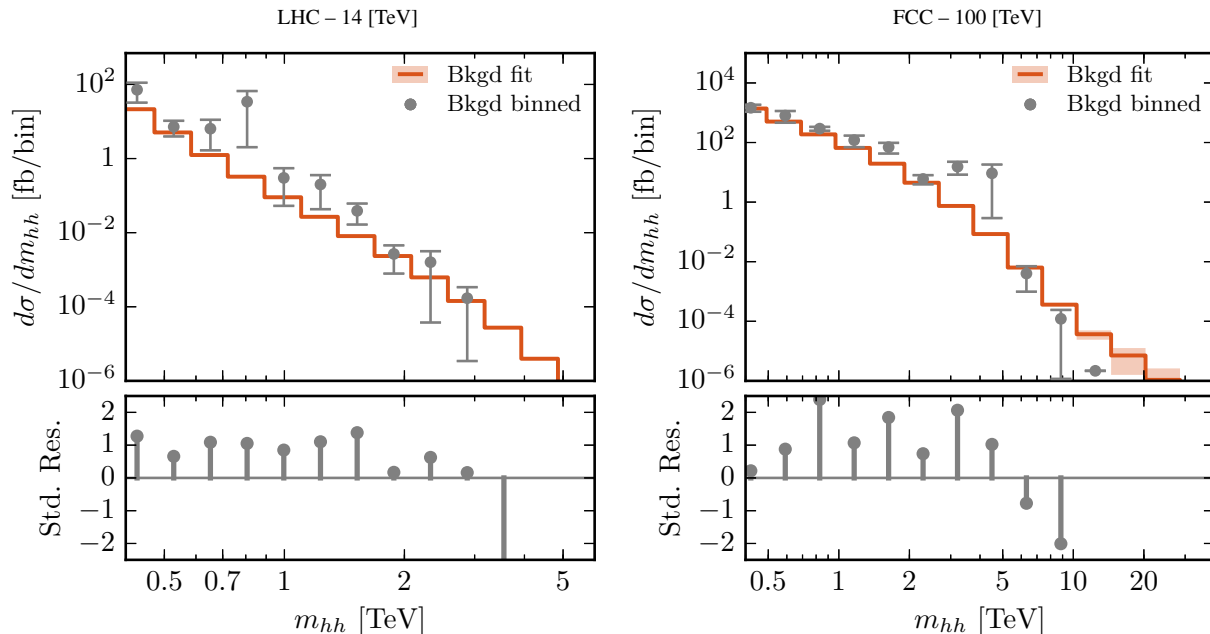


Fig. 15 Invariant mass distribution of the di-Higgs system for the total background at 14 TeV (left) and 100 TeV (right). The histograms are obtained by summing the contributions from the separate fits to each background processes. We also show the binned MC events (filled circles) with their statistical uncertainty. The lower panels show the standardized residuals in each bin.

Appendix C: Validation of the QCD multijet generation

As discussed in Appendix A, the modelling of the tail of the m_{hh} distribution for background processes is particularly challenging. One reason is because all the backgrounds considered are characterized by a steep power-like fall-off with m_{hh} above the di-Higgs production threshold, and therefore it becomes necessary to introduce a cross-section parametrization (see Appendix B) to be able to cover this region.

In addition, in the case of the QCD multijet backgrounds, there are different options available for the modelling of the m_{hh} distribution, in particular the multiplicity of the matrix-element calculation prior to the parton shower. Ideally, one should generate all relevant final-state partonic multiplicities and merge them to avoid double counting, either at LO [127, 128, 129] or at NLO [130, 131]. For the purposes of this feasibility study, however, we found it sufficient to generate LO samples using $4b$ and $2b2j$ matrix elements with Sherpa, with additional hard radiation provided by the parton shower. Note that our approach could introduce some double counting from gluon splittings into $b\bar{b}$, which if anything would increase the background cross section and make our estimates of $\delta_{c_{2V}}$ more conservative. Moreover, let us recall that, as discussed in Sec. 4, an actual experimental analysis would estimate the overall background normalization by means of data-driven techniques.

To validate the robustness of our simulation of the m_{hh} distributions for the QCD multijet background, we have compared the Sherpa calculation, based on $4b$ and $2b2j$ matrix elements and weighted events, with the ALPGEN simulation, based on $4b2j$ and $2b4j$ matrix elements and unweighted events showered with Pythia8. In principle, ALPGEN should provide a better description of the kinematics of the VBF jets, since it is based on higher-multiplicity matrix elements, but it has the drawback that populating the tail of the m_{hh} with unweighted events is very CPU-time intensive. On the other hand, it turns out that the two approaches give comparable results for the m_{hh} distribution in the region where both approaches lead to sufficient MC statistics, validating the use of the Sherpa for the calculation of background cross sections.

In Fig. 16 we show the m_{hh} distribution for the $4b$ background at 14 TeV and 100 TeV, comparing the ALPGEN and SHERPA calculations. We find good agreement for the entire m_{hh} range, indicating that the SHERPA event generation does a reasonable job in modelling the VBF tagging jets, and demonstrating that it can be reliably used to populate the large m_{hh} region for the multijet backgrounds with high efficiency. The differences between the two calculations are at most a factor two, typically less, well within the typical size of the theoretical uncertainties for LO multijet calculations.

Figure 17 shows a similar comparison for the invariant mass of the two VBF tagging jets, m_{jj} , and for the transverse momentum of the hardest light jet in the event, p_{Tj_1} . For the m_{jj} distribution, the agreement between the ALPGEN and

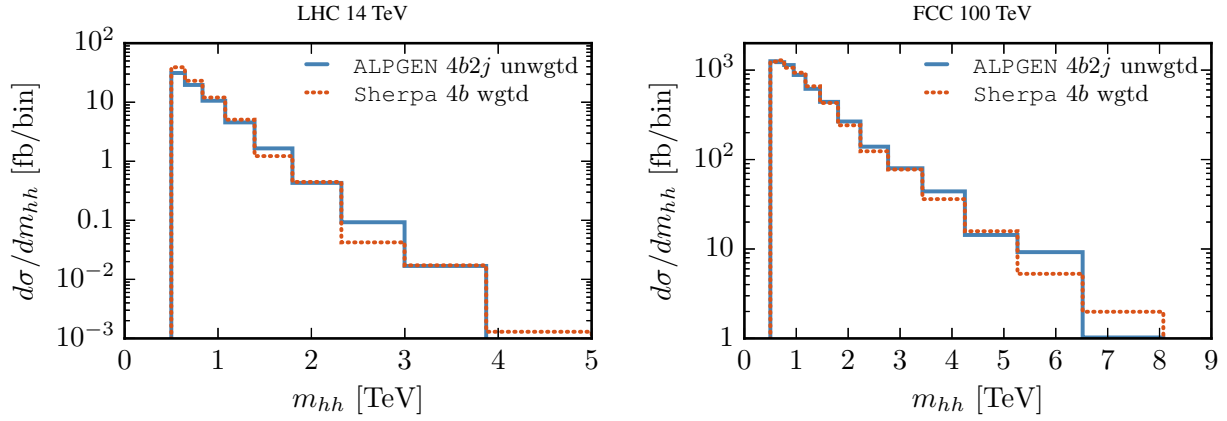


Fig. 16 Di-Higgs invariant mass distribution for the $4b$ background, comparing the results of ALPGEN, where unweighted events are generated with $4b2j$ matrix elements, with those of SHERPA, where weighted events are generated with $4b$ matrix elements, at 14 TeV (left) and 100 TeV (right).

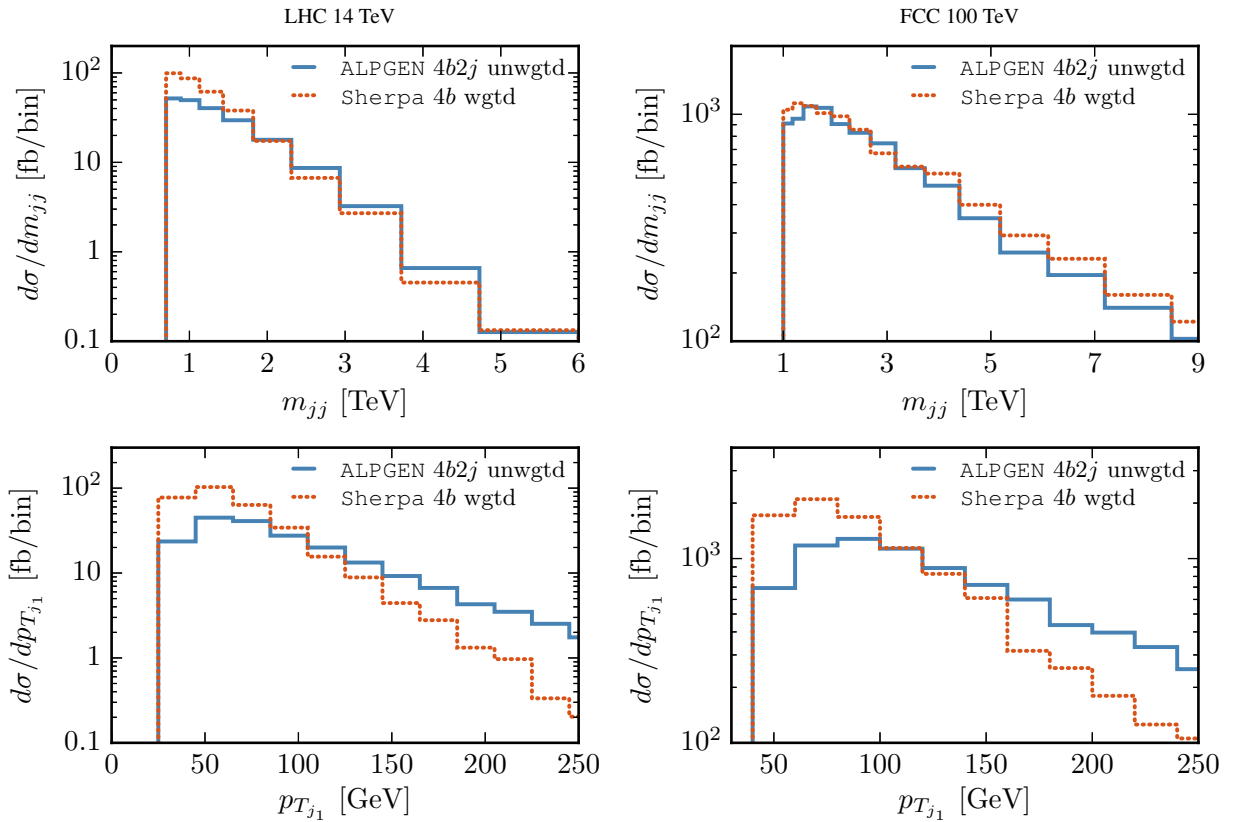


Fig. 17 Same as Fig. 16, now for the invariant mass of the two VBF tagging jets m_{jj} (upper plots) and the transverse momentum of the hardest light jet in the event p_{Tj_1} (upper plots).

SHERPA calculations is also good for the entire kinematical range. On the other hand, for the transverse momentum of the leading jet the ALPGEN calculation leads to harder (softer) spectra than the SHERPA one at high (low) values of p_{Tj_1} . This can be understood from the fact that j_1 will be typically generated by the parton shower in the latter case, and by the matrix element in the former. These differences are however inconsequential for our analysis, since the cuts imposed on the p_T of the VBF tagging jets are relatively mild, see Table 2, and thus the event selection will not be affected.

The validation studies discussed in this Appendix demonstrate that, for the purposes of the present analysis, our approach to event generation based on SHERPA for the simulation of the QCD multijet backgrounds is justified. On

Bin	σ_{SM} [fb]	A	B	$\rho_{\sigma A}$	$\rho_{\sigma B}$	ρ_{AB}
1	$(3.08 \pm 0.05) \times 10^{-4}$	-3.61 ± 0.0957	6.89 ± 0.217	0.3	-0.62	-0.66
2	$(5.84 \pm 0.0691) \times 10^{-4}$	-3.96 ± 0.0706	7.27 ± 0.161	0.32	-0.62	-0.68
3	$(7.17 \pm 0.0654) \times 10^{-4}$	-4.3 ± 0.0573	9.71 ± 0.148	0.32	-0.68	-0.63
4	$(7.31 \pm 0.049) \times 10^{-4}$	-4.96 ± 0.0462	14.9 ± 0.146	0.35	-0.77	-0.59
5	$(5.98 \pm 0.0507) \times 10^{-4}$	-6.39 ± 0.0677	26.7 ± 0.287	0.42	-0.86	-0.59
6	$(4.19 \pm 0.0677) \times 10^{-4}$	-8.28 ± 0.157	50.1 ± 0.93	0.5	-0.92	-0.6
7	$(2.38 \pm 0.0571) \times 10^{-4}$	-11.9 ± 0.302	103 ± 2.65	0.61	-0.96	-0.67
8	$(1.15 \pm 0.0447) \times 10^{-4}$	-15.1 ± 0.597	174 ± 7.05	0.67	-0.98	-0.71
9	$(4.93 \pm 0.176) \times 10^{-5}$	-19.4 ± 0.712	301 ± 11	0.72	-0.99	-0.75
10	$(1.68 \pm 0.148) \times 10^{-5}$	-29.1 ± 2.65	758 ± 67.8	0.8	-1	-0.81
11	$(5.41 \pm 1.02) \times 10^{-6}$	-42.3 ± 8.58	$1.69 \times 10^3 \pm 320$	0.83	-1	-0.83
12	$(1.28 \pm 0.506) \times 10^{-6}$	-47.4 ± 22.6	$(3.88 \pm 1.53) \times 10^3$	0.76	-1	-0.77
13	$(8.55 \pm 13.4) \times 10^{-7}$	-16.5 ± 29.7	$(2.27 \pm 3.57) \times 10^3$	0.76	-1	-0.77
14	$(3.5 \pm 3.57) \times 10^{-7}$	-0.00901 ± 26.4	$(1.28 \pm 1.31) \times 10^3$	-0.064	-1	0.055
15	$(6.24 \pm 3.38) \times 10^{-7}$	-3.59 ± 5.3	105 ± 60.7	0.19	-0.98	-0.24
16	$(6.33 \pm 1.97) \times 10^{-7}$	-2.88 ± 1.57	22.1 ± 8.59	0.15	-0.9	-0.36

Table 11 The bin by bin fit coefficients obtained by fitting MC events to Eq. (7) for the LHC with $\sqrt{s} = 14$ TeV. The first column labelled ‘Bin’ gives the bin number in question. The bin definition is given in the text, see also footnote 2. The last three columns labelled ρ_{0A} , ρ_{0B} , and ρ_{AB} give the coefficients of the correlation matrix among the three fit parameters.

the other hand, they also highlight that future studies aiming to enhance the separation between signal and background events from shape comparisons of kinematical distributions, such as multivariate analysis [43], would require an improved modeling of the QCD multijet backgrounds. This could be achieved by using merging techniques to combine QCD jet samples of different multiplicities.

Appendix D: Coefficients of the $\delta_{c_{2V}}$ fit

The dependence of the signal cross section on $\delta_{c_{2V}}$, as parametrized in Eq. (7), is required in order to construct the likelihood function. In this appendix, we list the coefficients of Eq. (7) in each m_{hh} bin. The coefficients are extracted by fitting MC events after all cuts have been applied as discussed in Sec. 3 with the exception of the m_{hh} cut. We use 15 equally spaced bins on a log scale starting from 250 GeV up to 6(30) TeV for $\sqrt{s} = 14(100)$ TeV. In addition, we define an overflow bin up to the centre of mass energy. The results are shown in Tabs. 11 and 12. The fit error on each coefficient is also provided along with the off-diagonal entries of the correlation matrix ρ_{ij} where $i, j \in \{\sigma, A, B\}$.

References

1. G. Aad, et al., Phys. Lett. **B716**, 1 (2012). DOI 10.1016/j.physletb.2012.08.020
2. S. Chatrchyan, et al., Phys. Lett. **B716**, 30 (2012). DOI 10.1016/j.physletb.2012.08.021
3. G.F. Giudice, C. Grojean, A. Pomarol, R. Rattazzi, JHEP **06**, 045 (2007). DOI 10.1088/1126-6708/2007/06/045
4. R. Contino, C. Grojean, M. Moretti, F. Piccinini, R. Rattazzi, JHEP **05**, 089 (2010). DOI 10.1007/JHEP05(2010)089
5. R. Contino, C. Grojean, D. Pappadopulo, R. Rattazzi, A. Thamm, JHEP **02**, 006 (2014). DOI 10.1007/JHEP02(2014)006
6. A. Belyaev, M. Drees, O.J.P. Eboli, J.K. Mizukoshi, S.F. Novaes, in *Proceedings, International Europhysics Conference on High energy physics (EPS-HEP 1999): Tampere, Finland, July 15-21, 1999* (1999), pp. 748–751. URL <http://alice.cern.ch/format/showfull?sysnb=0330978>
7. B. Grinstein, M. Trott, Phys. Rev. **D76**, 073002 (2007). DOI 10.1103/PhysRevD.76.073002
8. R. Grober, M. Muhlleitner, JHEP **06**, 020 (2011). DOI 10.1007/JHEP06(2011)020
9. J. Cao, Z. Heng, L. Shang, P. Wan, J.M. Yang, JHEP **04**, 134 (2013). DOI 10.1007/JHEP04(2013)134
10. M. Gouzevitch, A. Oliveira, J. Rojo, R. Rosenfeld, G.P. Salam, V. Sanz, JHEP **07**, 148 (2013). DOI 10.1007/JHEP07(2013)148
11. R. Barbieri, D. Buttazzo, K. Kannike, F. Sala, A. Tesi, Phys. Rev. **D87**(11), 115018 (2013). DOI 10.1103/PhysRevD.87.115018
12. U. Ellwanger, JHEP **08**, 077 (2013). DOI 10.1007/JHEP08(2013)077
13. C. Han, X. Ji, L. Wu, P. Wu, J.M. Yang, JHEP **04**, 003 (2014). DOI 10.1007/JHEP04(2014)003
14. J.M. No, M. Ramsey-Musolf, Phys. Rev. **D89**(9), 095031 (2014). DOI 10.1103/PhysRevD.89.095031
15. B. Hespel, D. Lopez-Val, E. Vryonidou, JHEP **09**, 124 (2014). DOI 10.1007/JHEP09(2014)124

Bin	σ_{SM} [fb]	A	B	$\rho_{\sigma A}$	$\rho_{\sigma B}$	ρ_{AB}
1	$(5.98 \pm 0.152) \times 10^{-3}$	-2.87 ± 0.191	7.8 ± 0.513	0.14	-0.57	-0.35
2	$(1.43 \pm 0.0185) \times 10^{-2}$	-4.29 ± 0.106	11.8 ± 0.317	0.23	-0.62	-0.46
3	$(2.25 \pm 0.0246) \times 10^{-2}$	-5.63 ± 0.0999	21.9 ± 0.395	0.29	-0.74	-0.46
4	$(2.36 \pm 0.045) \times 10^{-2}$	-7.95 ± 0.212	50.8 ± 1.27	0.37	-0.86	-0.47
5	$(1.88 \pm 0.0277) \times 10^{-2}$	-11.7 ± 0.203	109 ± 1.86	0.5	-0.93	-0.56
6	$(1.14 \pm 0.0226) \times 10^{-2}$	-14.6 ± 0.339	210 ± 4.5	0.56	-0.97	-0.6
7	$(5.68 \pm 0.196) \times 10^{-3}$	-24.9 ± 0.985	729 ± 25.8	0.69	-0.99	-0.7
8	$(2.73 \pm 0.224) \times 10^{-3}$	-43.2 ± 4.07	$2.05 \times 10^3 \pm 170$	0.77	-1	-0.78
9	$(1.1 \pm 0.104) \times 10^{-3}$	-61.3 ± 7.08	$5.54 \times 10^3 \pm 523$	0.77	-1	-0.77
10	$(2.97 \pm 0.806) \times 10^{-4}$	-135 ± 43.2	$(1.96 \pm 0.532) \times 10^4$	0.83	-1	-0.83
11	$(4.83 \pm 2.99) \times 10^{-5}$	-66.2 ± 124	$(9.7 \pm 6.01) \times 10^4$	0.32	-1	-0.32
12	$(1.71 \pm 1.57) \times 10^{-5}$	-114 ± 276	$(1.88 \pm 1.73) \times 10^5$	0.37	-1	-0.37
13	$(1.39 \pm 31.2) \times 10^{-5}$	$-163 \pm 3.64 \times 10^3$	$(1.21 \pm 27.3) \times 10^5$	1	-1	-1
14	$(4.32 \pm 219) \times 10^{-6}$	-1.59 ± 689	$(1.35 \pm 68.1) \times 10^5$	-0.012	-1	0.012
15	$(2.66 \pm 6.97) \times 10^{-5}$	-0.0026 ± 32.2	$(3.53 \pm 9.29) \times 10^3$	-0.091	-1	0.09
16	$(2.6 \pm 1.8) \times 10^{-5}$	-0.0018 ± 7.38	144 ± 109	-0.38	-0.98	0.36

Table 12 Same as Tab. 11 but for the FCC with $\sqrt{s} = 100$ TeV.

16. J. Cao, D. Li, L. Shang, P. Wu, Y. Zhang, JHEP **12**, 026 (2014). DOI 10.1007/JHEP12(2014)026
17. A. Azatov, R. Contino, G. Panico, M. Son, Phys. Rev. **D92**(3), 035001 (2015). DOI 10.1103/PhysRevD.92.035001
18. D. Buttazzo, F. Sala, A. Tesi, JHEP **11**, 158 (2015). DOI 10.1007/JHEP11(2015)158
19. W.J. Zhang, W.G. Ma, R.Y. Zhang, X.Z. Li, L. Guo, C. Chen, Phys. Rev. **D92**, 116005 (2015). DOI 10.1103/PhysRevD.92.116005
20. L. Wu, J.M. Yang, C.P. Yuan, M. Zhang, Phys. Lett. **B747**, 378 (2015). DOI 10.1016/j.physletb.2015.06.020
21. G. Aad, et al., Phys. Rev. Lett. **114**(8), 081802 (2015). DOI 10.1103/PhysRevLett.114.081802
22. V. Khachatryan, et al., Phys. Lett. **B749**, 560 (2015). DOI 10.1016/j.physletb.2015.08.047
23. G. Aad, et al., Eur. Phys. J. **C75**(9), 412 (2015). DOI 10.1140/epjc/s10052-015-3628-x
24. G. Aad, et al., Phys. Rev. **D92**, 092004 (2015). DOI 10.1103/PhysRevD.92.092004
25. V. Khachatryan, et al., Phys. Lett. **B755**, 217 (2016). DOI 10.1016/j.physletb.2016.01.056
26. ATLAS Collaboration, Search for Higgs boson pair production in the final state of $\gamma\gamma WW^*(\rightarrow lvjj)$ using 13.3 fb $^{-1}$ of pp collision data recorded at $\sqrt{s} = 13$ TeV with the ATLAS detector. Tech. Rep. ATLAS-CONF-2016-071 (2016). URL <http://cds.cern.ch/record/2206222>
27. M. Aaboud, et al., Phys. Rev. **D94**(5), 052002 (2016). DOI 10.1103/PhysRevD.94.052002
28. CMS Collaboration, Search for heavy resonances decaying to a pair of Higgs bosons in four b quark final state in proton-proton collisions at $\sqrt{s}=13$ TeV (2016). URL <https://cds.cern.ch/record/2202811?ln=en>
29. CMS Collaboration, Search for Higgs boson pair production in the $b\bar{b}lv$ final state at $\sqrt{s} = 13$ TeV (2016). URL <https://cds.cern.ch/record/2205782>
30. W. Yao, Studies of measuring Higgs self-coupling with $HH \rightarrow b\bar{b}\gamma\gamma$ at the future hadron colliders. Tech. rep. (2013). URL <http://inspirehep.net/record/1251544/files/arXiv:1308.6302.pdf>
31. A.J. Barr, M.J. Dolan, C. Englert, D.E. Ferreira de Lima, M. Spannowsky, JHEP **02**, 016 (2015). DOI 10.1007/JHEP02(2015)016
32. A. Papaefstathiou, Phys. Rev. **D91**(11), 113016 (2015). DOI 10.1103/PhysRevD.91.113016
33. N. Arkani-Hamed, T. Han, M. Mangano, L.T. Wang, Phys. Rept. **652**, 1 (2016). DOI 10.1016/j.physrep.2016.07.004
34. R. Contino, et al., Physics at a 100 TeV pp collider: Higgs and EW symmetry breaking studies. Tech. rep. (2016)
35. D. de Florian, et al., Handbook of LHC Higgs Cross Sections: 4. Deciphering the Nature of the Higgs Sector. Tech. rep. (2016)
36. M.J. Dolan, C. Englert, M. Spannowsky, JHEP **10**, 112 (2012). DOI 10.1007/JHEP10(2012)112
37. A. Papaefstathiou, L.L. Yang, J. Zurita, Phys. Rev. **D87**(1), 011301 (2013). DOI 10.1103/PhysRevD.87.011301
38. A.J. Barr, M.J. Dolan, C. Englert, M. Spannowsky, Phys. Lett. **B728**, 308 (2014). DOI 10.1016/j.physletb.2013.12.011
39. B. Cooper, N. Konstantinidis, L. Lambourne, D. Wardrope, Phys. Rev. **D88**(11), 114005 (2013). DOI 10.1103/PhysRevD.88.114005
40. C.T. Lu, J. Chang, K. Cheung, J.S. Lee, JHEP **08**, 133 (2015). DOI 10.1007/JHEP08(2015)133
41. D. Wardrope, E. Jansen, N. Konstantinidis, B. Cooper, R. Falla, N. Norjoharuddeen, Eur. Phys. J. **C75**(5), 219 (2015). DOI 10.1140/epjc/s10052-015-3439-0
42. D.E. Ferreira de Lima, A. Papaefstathiou, M. Spannowsky, JHEP **08**, 030 (2014). DOI 10.1007/JHEP08(2014)030
43. J.K. Behr, D. Bortoletto, J.A. Frost, N.P. Hartland, C. Issever, J. Rojo, Eur. Phys. J. **C76**(7), 386 (2016). DOI 10.1140/epjc/s10052-016-4215-5
44. S. Dawson, S. Dittmaier, M. Spira, Phys. Rev. **D58**, 115012 (1998). DOI 10.1103/PhysRevD.58.115012
45. D. de Florian, J. Mazzitelli, Phys. Rev. Lett. **111**, 201801 (2013). DOI 10.1103/PhysRevLett.111.201801
46. D.Y. Shao, C.S. Li, H.T. Li, J. Wang, JHEP **07**, 169 (2013). DOI 10.1007/JHEP07(2013)169
47. D. de Florian, J. Mazzitelli, JHEP **09**, 053 (2015). DOI 10.1007/JHEP09(2015)053
48. F. Maltoni, E. Vryonidou, M. Zaro, JHEP **11**, 079 (2014). DOI 10.1007/JHEP11(2014)079
49. J. Grigo, J. Hoff, K. Melnikov, M. Steinhauser, Nucl. Phys. **B875**, 1 (2013). DOI 10.1016/j.nuclphysb.2013.06.024
50. G. Degrandi, P.P. Giardino, R. Gr uber, Eur. Phys. J. **C76**(7), 411 (2016). DOI 10.1140/epjc/s10052-016-4256-9

51. S. Borowka, N. Greiner, G. Heinrich, S. Jones, M. Kerner, J. Schlenk, U. Schubert, T. Zirke, Phys. Rev. Lett. **117**(1), 012001 (2016). DOI 10.1103/PhysRevLett.117.079901, 10.1103/PhysRevLett.117.012001. [Erratum: Phys. Rev. Lett.117,no.7,079901(2016)]
52. P. Maierhöfer, A. Papaefstathiou, JHEP **03**, 126 (2014). DOI 10.1007/JHEP03(2014)126
53. R. Frederix, S. Frixione, V. Hirschi, F. Maltoni, O. Mattelaer, P. Torrielli, E. Vryonidou, M. Zaro, Phys. Lett. **B732**, 142 (2014). DOI 10.1016/j.physletb.2014.03.026
54. ATLAS Collaboration, *Prospects for measuring Higgs pair production in the channel $H(\rightarrow \gamma\gamma)H(\rightarrow b\bar{b})$ using the ATLAS detector at the HL-LHC*. Geneva (2014). URL <http://cds.cern.ch/record/1956733>
55. ATLAS Collaboration, *Higgs Pair Production in the $H(\rightarrow \tau\tau)H(\rightarrow b\bar{b})$ channel at the High-Luminosity LHC*. Geneva (2015). URL <http://cds.cern.ch/record/2065974>
56. CMS Collaboration, *Higgs pair production at the High Luminosity LHC* (2015). URL <https://cds.cern.ch/record/2063038?ln=en>
57. ATLAS Collaboration, *Projected sensitivity to non-resonant Higgs boson pair production in the $b\bar{b}b\bar{b}$ final state using proton-proton collisions at HL-LHC with the ATLAS detector*. Geneva (2016). URL <http://cds.cern.ch/record/2221658>
58. CMS Collaboration, *Updates on Projections of Physics Reach with the Upgraded CMS Detector for High Luminosity LHC* (2016). URL <https://cds.cern.ch/record/2221747>
59. F. Goertz, A. Papaefstathiou, L.L. Yang, J. Zurita, JHEP **06**, 016 (2013). DOI 10.1007/JHEP06(2013)016
60. M. Slawinska, W. van den Wollenberg, B. van Eijk, S. Bentvelsen, Phenomenology of the trilinear Higgs coupling at proton-proton colliders. Tech. rep. (2014)
61. M.J. Dolan, C. Englert, N. Greiner, M. Spannowsky, Phys. Rev. Lett. **112**, 101802 (2014). DOI 10.1103/PhysRevLett.112.101802
62. G. Brooijmans, et al., Les Houches 2013: Physics at TeV Colliders: New Physics Working Group Report. Tech. rep. (2014)
63. L.S. Ling, R.Y. Zhang, W.G. Ma, L. Guo, W.H. Li, X.Z. Li, Phys. Rev. **D89**(7), 073001 (2014). DOI 10.1103/PhysRevD.89.073001
64. M.J. Dolan, C. Englert, N. Greiner, K. Nordstrom, M. Spannowsky, Eur. Phys. J. **C75**(8), 387 (2015). DOI 10.1140/epjc/s10052-015-3622-3
65. J. Baglio, A. Djouadi, R. Gröber, M.M. Mühlleitner, J. Quevillon, M. Spira, JHEP **04**, 151 (2013). DOI 10.1007/JHEP04(2013)151
66. V.D. Barger, T. Han, R.J.N. Phillips, Phys. Rev. **D38**, 2766 (1988). DOI 10.1103/PhysRevD.38.2766
67. Q.H. Cao, Y. Liu, B. Yan, Phys. Rev. **D95**(7), 073006 (2017). DOI 10.1103/PhysRevD.95.073006
68. C. Englert, F. Krauss, M. Spannowsky, J. Thompson, Phys. Lett. **B743**, 93 (2015). DOI 10.1016/j.physletb.2015.02.041
69. D.B. Kaplan, H. Georgi, Phys. Lett. **B136**, 183 (1984). DOI 10.1016/0370-2693(84)91177-8
70. J. Nakamura, J. Baglio, Eur. Phys. J. **C77**(1), 35 (2017). DOI 10.1140/epjc/s10052-017-4593-3
71. G.P. Salam, Eur. Phys. J. **C67**, 637 (2010). DOI 10.1140/epjc/s10052-010-1314-6
72. G. Aad, et al., Phys. Rev. Lett. **114**, 191803 (2015). DOI 10.1103/PhysRevLett.114.191803
73. M.S. Chanowitz, M.K. Gaillard, Nucl. Phys. **B261**, 379 (1985). DOI 10.1016/0550-3213(85)90580-2
74. V. Khachatryan, et al., Eur. Phys. J. **C74**(10), 3076 (2014). DOI 10.1140/epjc/s10052-014-3076-z
75. G. Aad, et al., Phys. Lett. **B753**, 69 (2016). DOI 10.1016/j.physletb.2015.11.071
76. G. Aad, et al., Eur. Phys. J. **C76**(1), 6 (2016). DOI 10.1140/epjc/s10052-015-3769-y
77. J.R. Espinosa, C. Grojean, M. Mühlleitner, M. Trott, JHEP **12**, 045 (2012). DOI 10.1007/JHEP12(2012)045
78. J. Ellis, T. You, JHEP **06**, 103 (2013). DOI 10.1007/JHEP06(2013)103
79. A. Pomarol, F. Riva, JHEP **01**, 151 (2014). DOI 10.1007/JHEP01(2014)151
80. M. Ciuchini, E. Franco, S. Mishima, L. Silvestrini, JHEP **08**, 106 (2013). DOI 10.1007/JHEP08(2013)106
81. K. Agashe, R. Contino, A. Pomarol, Nucl. Phys. **B719**, 165 (2005). DOI 10.1016/j.nuclphysb.2005.04.035
82. R. Contino, L. Da Rold, A. Pomarol, Phys. Rev. **D75**, 055014 (2007). DOI 10.1103/PhysRevD.75.055014
83. E. Halyo, Mod. Phys. Lett. **A8**, 275 (1993). DOI 10.1142/S0217732393000271
84. W.D. Goldberger, B. Grinstein, W. Skiba, Phys. Rev. Lett. **100**, 111802 (2008). DOI 10.1103/PhysRevLett.100.111802
85. L. Vecchi, Phys. Rev. **D82**, 076009 (2010). DOI 10.1103/PhysRevD.82.076009
86. B.A. Campbell, J. Ellis, K.A. Olive, JHEP **03**, 026 (2012). DOI 10.1007/JHEP03(2012)026
87. Z. Chacko, R. Franceschini, R.K. Mishra, JHEP **04**, 015 (2013). DOI 10.1007/JHEP04(2013)015
88. B. Bellazzini, C. Csaki, J. Hubisz, J. Serra, J. Terning, Eur. Phys. J. **C73**(2), 2333 (2013). DOI 10.1140/epjc/s10052-013-2333-x
89. N. Craig, H.K. Lou, M. McCullough, A. Thalappillil, JHEP **02**, 127 (2016). DOI 10.1007/JHEP02(2016)127
90. K. Assamagan, et al., in *The Higgs Portal and Cosmology* (2016). URL <https://inspirehep.net/record/1449094/files/arXiv:1604.05324.pdf>
91. R. Contino, D. Marzocca, D. Pappadopulo, R. Rattazzi, JHEP **10**, 081 (2011). DOI 10.1007/JHEP10(2011)081
92. B. Bellazzini, C. Csaki, J. Hubisz, J. Serra, J. Terning, JHEP **11**, 003 (2012). DOI 10.1007/JHEP11(2012)003
93. E. Accomando, L. Fedeli, S. Moretti, S. De Curtis, D. Dominici, Phys. Rev. **D86**, 115006 (2012). DOI 10.1103/PhysRevD.86.115006
94. A.E. Carcamo Hernandez, C.O. Dib, A.R. Zerwekh, Eur. Phys. J. **C74**, 2822 (2014). DOI 10.1140/epjc/s10052-014-2822-6
95. D. Greco, D. Liu, JHEP **12**, 126 (2014). DOI 10.1007/JHEP12(2014)126
96. D. Pappadopulo, A. Thamm, R. Torre, A. Wulzer, JHEP **09**, 060 (2014). DOI 10.1007/JHEP09(2014)060
97. R. Contino, A. Falkowski, F. Goertz, C. Grojean, F. Riva, JHEP **07**, 144 (2016). DOI 10.1007/JHEP07(2016)144
98. M. Cacciari, G.P. Salam, G. Soyez, Eur. Phys. J. **C72**, 1896 (2012). DOI 10.1140/epjc/s10052-012-1896-2
99. M. Cacciari, G.P. Salam, G. Soyez, JHEP **04**, 063 (2008). DOI 10.1088/1126-6708/2008/04/063
100. S. Chatrchyan, et al., *Results on b-tagging identification in 8 TeV pp collisions* (2013). URL <https://cds.cern.ch/record/1528183>
101. CMS Collaboration, *Performance of b tagging at $\sqrt{s}=8$ TeV in multijet, $t\bar{t}$ and boosted topology events*. Geneva (2013). URL <https://cds.cern.ch/record/1581306>
102. ATLAS Collaboration, *Flavor Tagging with Track Jets in Boosted Topologies with the ATLAS Detector* (2014). URL <https://cds.cern.ch/record/1750681>
103. G. Aad, et al., *b-tagging in dense environments* (2014). URL <https://cds.cern.ch/record/1750682?ln=en>
104. CMS Collaboration, *b-tagging in boosted topologies* (2015). URL <http://cds.cern.ch/record/2048095>
105. Y.L. Dokshitzer, G.D. Leder, S. Moretti, B.R. Webber, JHEP **08**, 001 (1997). DOI 10.1088/1126-6708/1997/08/001
106. J.M. Butterworth, A.R. Davison, M. Rubin, G.P. Salam, Phys. Rev. Lett. **100**, 242001 (2008). DOI 10.1103/PhysRevLett.100.242001
107. B.T. Huffman, C. Jackson, J. Tseng, J. Phys. **G43**(8), 085001 (2016). DOI 10.1088/0954-3899/43/8/085001
108. M. Selvaggi. Fcc-hh detector concept, simulation activities and physics benchmarks. https://indico.cern.ch/event/550509/contributions/2413234/attachments/1395960/2128279/ccphysics_week_v4.pdf

109. G. D'Agostini, *Bayesian reasoning in data analysis: A critical introduction* (World Scientific, New Jersey, USA, 2003)
110. M. Aaboud, et al., *Eur. Phys. J.* **C76**(12), 670 (2016). DOI 10.1140/epjc/s10052-016-4521-y
111. ATLAS Collaboration, *Projections for measurements of Higgs boson signal strengths and coupling parameters with the ATLAS detector at a HL-LHC*. Geneva (2014). URL <http://cds.cern.ch/record/1956710>
112. J. Alwall, R. Frederix, S. Frixione, V. Hirschi, F. Maltoni, O. Mattelaer, H.S. Shao, T. Stelzer, P. Torrielli, M. Zaro, *JHEP* **07**, 079 (2014). DOI 10.1007/JHEP07(2014)079
113. C. Degrande, C. Duhr, B. Fuks, D. Grellscheid, O. Mattelaer, T. Reiter, *Comput. Phys. Commun.* **183**, 1201 (2012). DOI 10.1016/j.cpc.2012.01.022
114. A. Alloul, B. Fuks, V. Sanz, *JHEP* **04**, 110 (2014). DOI 10.1007/JHEP04(2014)110
115. P. Artoisenet, et al., *JHEP* **11**, 043 (2013). DOI 10.1007/JHEP11(2013)043
116. R.D. Ball, et al., *Nucl. Phys.* **B867**, 244 (2013). DOI 10.1016/j.nuclphysb.2012.10.003
117. A. Buckley, J. Ferrando, S. Lloyd, K. Nordström, B. Page, M. Rufenacht, M. SchÅnherr, G. Watt, *Eur. Phys. J.* **C75**, 132 (2015). DOI 10.1140/epjc/s10052-015-3318-8
118. T. Sjöstrand, S. Ask, J.R. Christiansen, R. Corke, N. Desai, P. Ilten, S. Mrenna, S. Prestel, C.O. Rasmussen, P.Z. Skands, *Comput. Phys. Commun.* **191**, 159 (2015). DOI 10.1016/j.cpc.2015.01.024
119. P. Skands, S. Carrazza, J. Rojo, *Eur. Phys. J.* **C74**(8), 3024 (2014). DOI 10.1140/epjc/s10052-014-3024-y
120. M. Cacciari, G.P. Salam, G. Soyez, *Eur. Phys. J.* **C75**(2), 59 (2015). DOI 10.1140/epjc/s10052-015-3267-2
121. M.L. Mangano, M. Moretti, F. Piccinini, R. Pittau, A.D. Polosa, *JHEP* **07**, 001 (2003). DOI 10.1088/1126-6708/2003/07/001
122. M. Czakon, P. Fiedler, A. Mitov, *Phys. Rev. Lett.* **110**, 252004 (2013). DOI 10.1103/PhysRevLett.110.252004
123. T. Gleisberg, S. Hoeche, F. Krauss, M. Schonherr, S. Schumann, F. Siegert, J. Winter, *JHEP* **02**, 007 (2009). DOI 10.1088/1126-6708/2009/02/007
124. R.D. Ball, et al., *JHEP* **04**, 040 (2015). DOI 10.1007/JHEP04(2015)040
125. V. Hirschi, O. Mattelaer, *JHEP* **10**, 146 (2015). DOI 10.1007/JHEP10(2015)146
126. J.H. Davis, M. Fairbairn, J. Heal, P. Tunney, *The Significance of the 750 GeV Fluctuation in the ATLAS Run 2 Diphoton Data*. Tech. rep. (2016)
127. M.L. Mangano, M. Moretti, R. Pittau, *Nucl. Phys.* **B632**, 343 (2002). DOI 10.1016/S0550-3213(02)00249-3
128. S. Catani, F. Krauss, R. Kuhn, B.R. Webber, *JHEP* **11**, 063 (2001). DOI 10.1088/1126-6708/2001/11/063
129. J. Alwall, et al., *Eur. Phys. J.* **C53**, 473 (2008). DOI 10.1140/epjc/s10052-007-0490-5
130. S. Hoeche, F. Krauss, M. Schonherr, F. Siegert, *JHEP* **04**, 027 (2013). DOI 10.1007/JHEP04(2013)027
131. R. Frederix, S. Frixione, *JHEP* **12**, 061 (2012). DOI 10.1007/JHEP12(2012)061